2023-05-01

The Role of Near-Façade Flow in Wind-Dominant Single-Sided Natural Ventilation for an Isolated Three-Storey Building: An LES Study

Nima Najafi Ziarani

Malcolm J. Cook

Farnood Freidooni

Paul D. O'Sullivan

Building and Environment 235 (2023) 110210

Contents lists available at ScienceDirect

Building and Environment

journal homepage: www.elsevier.com/locate/buildenv

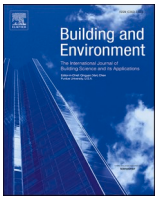

The role of near-façade flow in wind-dominant single-sided natural ventilation for an isolated three-storey building: An LES study

Nima Najafi Ziarani [a,b], Malcolm J. Cook [c], Farnood Freidooni [d], Paul D. O'Sullivan [a,b,*]

[a] MaREI, The SFI Research Centre for Energy, Climate and Marine, Ireland
[b] School of Mechanical, Electrical, and Process Engineering, Munster Technological University, Bishopstown, Cork, Ireland
[c] School of Architecture, Building and Civil Engineering, Loughborough University, Epinal Way, Loughborough, Leicestershire, LE11 3TU, United Kingdom
[d] Department of Mechanical Engineering, Isfahan University of Technology, Isfahan, 84156-83111, Iran

ARTICLE INFO

Keywords:
Single-sided
Natural ventilation
Computational fluid dynamics
Large eddy simulations
Mixing layer
Near-façade flow

ABSTRACT

Wind-driven single-sided ventilation is present in many existing buildings globally, and its performance can be unreliable and challenging to improve. To address these performance challenges, a better understanding of the interconnected relationship between the external and internal flows is required. Therefore, a detailed assessment of this type of natural ventilation is vital. A detailed CFD analysis of wind-dominant single-sided natural ventilation is presented by adopting the Large Eddy Simulation method, validated using previous wind tunnel studies. An isolated cube, representing a three-storey building, was used to investigate four case studies with different opening positions on the building façade. The presence of parallel flow near the building façade and the effect this has, both on the structure of the flow at the opening and the internal secondary flow, is investigated. Results demonstrate that a mixing layer jet of air is the main structure of the flow at the opening. The flow characteristics of this jet are a function of how the external near-façade flow interacts with the building. It can be deflected or attenuated by the near-façade fluctuating pressure and vortex structures close to the opening. Tracer gas decay results show that only 3/5 of the flow at the opening contributes to effective ventilation in this type of natural ventilation. Comparisons between the ventilation rates for openings at different positions on the building façade demonstrate the importance of the pressure role at the opening in single-sided natural ventilation.

1. Introduction

Nowadays, effective Natural Ventilation (NV) is highly valued, especially in mild and tropical climates [1], because it can effectively control indoor environments without using non-renewable energy [2,3]. Despite being a widely prevalent ventilation strategy, single-sided natural ventilation (SSV) systems must perform better to reduce their vulnerability [4] and ensure healthy indoor environments [5] with adequate indoor air quality and thermal comfort.

1.1. Background and context

Designing NV systems can present a greater challenge than designing their mechanically ventilated counterpart [6–12]. Therefore, as its performance varies stochastically, a detailed simulation-based assessment of the mechanisms that contribute to effective NV is valuable [8–10,13,14]. Ventilating naturally through an external opening can occur either due to wind or buoyancy-driven forces or the combined effect of both [2,10]. Wind-dominant NV through windows can be classified as single-sided ventilation (with one opening (SS1), or with two or more openings (SSn)), Cross Ventilation, and Corner Ventilation [15]. While cross ventilation can only be used in narrow-plan buildings with no large obstacles in the air path [16], SSV is perhaps the most common form of ventilation in modern apartments and offices because it can be easily implemented in buildings. Given its near ubiquitous adoption across residential and non-residential buildings, it is essential to understand the natural ventilation performance of SSV [16,17].

In SS1 and SS2 enclosures, when wind and stack effects are cancelling each other, the effect of fluctuating infiltration is significant due to the low mean pressure differences across the opening(s) and high turbulent components of pressure [18]. A fluctuating ventilation rate is the result of continuous and variable airflow exchange across the opening [2,19,20], penetration of eddies [21] or turbulent diffusion [22], and pulsating flow [18]. Turbulent fluctuations induced by variations in external wind conditions result in continuous and variable airflow

* Corresponding author. MaREI, The SFI Research Centre for Energy, Climate and Marine, Ireland.
E-mail address: Paul.OSullivan@mtu.ie (P.D. O'Sullivan).

https://doi.org/10.1016/j.buildenv.2023.110210
Received 16 November 2022; Received in revised form 6 March 2023; Accepted 12 March 2023
Available online 15 March 2023

Nomenclature

A	Opening area (m^2)
a	Opening height (m)
ACR	Air Change Rate ($1/s$)
C	Local mass fraction of each species
C_D	Drag coefficient (-)
C_L	Lift coefficient (-)
C_P	Instantaneous pressure coefficient (-)
$\overline{C}_P$	Mean pressure coefficient (-)
C_{t_i}	CO_2 concentration at time t_i (ppm)
CFL	Courant-Friedrichs-Lewy number (-)
D	Mass diffusion coefficient (-)
$F_r = Q/U_H A$	Flow number (-)
F_D	Drag force (N)
F_L	Lift force (N)
f	Frequency ($1/s$)
FAC2	Factor of 2 of observations
FAC1.3	Factor of 1.3 of observations
H	Cubic building's height (m)
I_u	Turbulence intensity for streamwise direction (%)
L	Length scale of turbulence (m)
n_x	Number of grids in x-direction (-)
n_y	Number of grids in y-direction (-)
n_z	Number of grids in z-direction (-)
O_i	Observed (measured) value
P_i	Predicted value
$\overline{Q}$	Q-criterion ($1/s^2$)
Q_t	Instantaneous flow rate (m^3/s)
Q_{mean}	Mean flow rate (m^3/s)
Re_H	Reynolds number based on building height (-)
R^2	R-squared value (-)
s	distance between the centre of openings (m)
Sc_t	Turbulent Schmidt number (-)
$St = fH/U_H$	Strouhal number (-)
T	Flow time (s)
T^*	Normalized flow time (-)
Δt	Time-step size (s)
$\Delta t^* = \Delta t U_H/H$	Normalized time-step size (-)
U	streamwise air velocity (m/s)
U_H	streamwise air velocity at the building height (m/s)
u_i	Air velocity (m/s)
u^*_{ABL}	Atmospheric boundary layer friction velocity (m/s)
V	Room volume (m^3)
X	X coordinate (-)
$X^* = (X/H)$	Normalized X coordinate (-)
Δx_i	Cell size in i-direction (m)
Y	Y coordinate (-)
$Y^* = (Y/H)$	Normalized Y coordinate (-)
$Z^* = (Z/H)$	Normalized Z coordinate (-)
z	Vertical distance from the ground (m)
z_0	Aerodynamic roughness length (m)

Greek letters

β	blockage ratio (%)
Δ	Filter width (m)
δ	Smallest grid length normal to the building (m)
ε	Turbulence dissipation rate (m^2/s^3)
$\varepsilon^* = \varepsilon H/U_H^3$	Normalized turbulence dissipation rate (-)
κ	von Karman constant
k	Turbulent kinetic energy (m^2/s^2)
$k^* = k/U_H^2$	Normalized turbulence kinetic energy (-)
λ	Integral length scale (m)
μ_t	Turbulent diffusion
ν	Kinematic viscosity (m^2/s)
ν_t	Turbulent viscosity (m^2/s)
ρ	Air density (Kg/m^3)
$\lvert\overline{\Omega}_{ij}\rvert$	Mean vorticity magnitude ($1/s$)
ω_x	x-vorticity ($1/s$)
ω_y	y-vorticity ($1/s$)
ω_z	z-vorticity ($1/s$)
$\omega^*_x = \omega_x H/U_H$	Instantaneous normalized x-vorticity (-)
$\omega^*_y = \omega_y H/U_H$	Instantaneous normalised y-vorticity (-)
$\omega^*_z = \omega_z H/U_H$	Instantaneous normalized z-vorticity (-)
$\overline{\omega}^*_x = \overline{\omega}_x H/U_H$	Mean normalized x-vorticity (-)
$\overline{\omega}^*_y = \overline{\omega}_y H/U_H$	Mean normalized y-vorticity (-)
$\overline{\omega}^*_z = \overline{\omega}_z H/U_H$	Mean normalized z-vorticity (-)

exchange across the opening [2]. Eddy penetration refers to shear ventilation in which the flow is parallel to the opening [2] and causes additional air exchange across an opening due to the penetration of eddies [18,23–25]. The outdoor wind contains eddies of different sizes [26] and only an eddy with a scale smaller than the opening size can penetrate the room [21]. Pulsating flow is the result of bulk fluctuating flow due to turbulence in the pressure difference across the opening, which can make an opening perform as an inlet or outlet depending on the positive or negative pressure difference between indoor and outdoor environments [2,18].

Of all empirical models used to estimate ventilation rates for wind-dominant SS1, the one which uses the classical theory of the mixing layer [22] provides good results for common wind speed conditions [12, 27–29]. This empirical model is based on Eq. (1) for a given value of θ, i.e., $f\{\theta\} =$ constant, this constant is typically found to be in the range of 0.013–0.035 [22,30],

$$\frac{q_{eff}}{AU_H} = f\{\theta\} \tag{1}$$

This mechanism of air exchange, i.e., a mixing layer along the opening face, occurs due to the presence of parallel flow locally at the opening, which has been reported in previous field measurement studies [12,29], illustrated in Fig. 1.

Understanding these phenomena requires coupling external and internal flows in SSV. Coupling here requires an understanding of the flow characteristics in SS1 by finding the inter-connected relationships between external flow (including near-façade flow) with the internal flow (including flow locally at the opening and secondary indoor flow) in this type of natural ventilation. To fulfil this requirement, the present study employed Computational Fluid Dynamics (CFD) to simulate the airflow around a generic isolated three-storey building. Since SSV is substantially affected by fluctuating infiltration, and the importance of capturing instantaneous features of the flow has been indicated in some wind-dominant natural ventilation studies [13,25,31,32], CFD methods such as Reynolds Averaged Navier Stokes (RANS) by which only mean values of the flow will be modelled are incapable of capturing all the flow structures, especially the fluctuating characteristics of single-sided ventilation rates [13]. In contrast, Large Eddy Simulation (LES) can simulate laminar, transient, and fully developed turbulent flows. Moreover, the detailed turbulence information provided by LES can be used for various external and internal flow evaluations [11,33,34].

The flow around a three-dimensional bluff body is of great interest in engineering practice [35]. For instance, to study wind loads and vortex-induced oscillations on buildings, bridges and vehicles.

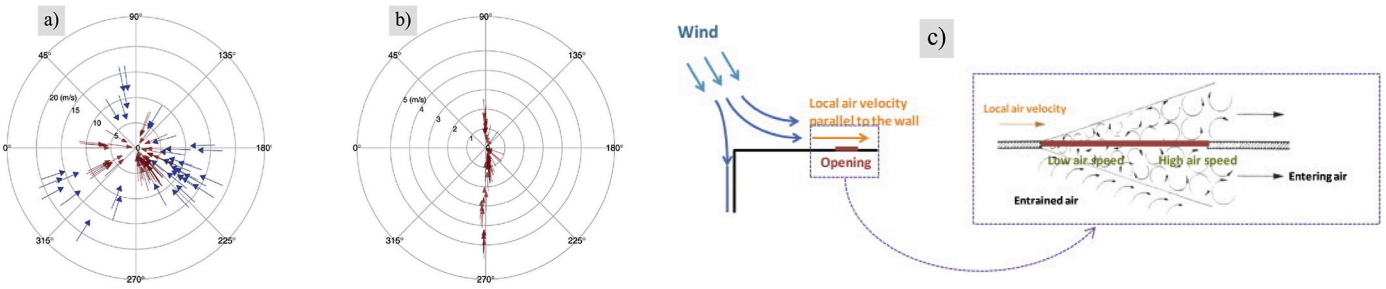

Fig. 1. Reported parallel flow in field measurements for single-sided natural ventilation even when the wind direction was windward, a and b. Note: a) is wind direction at the nearby meteorological weather station (blue), and 6 m above roof level (red) and b) is wind direction locally at the opening for the same conditions [29], c) *parallel flow locally at the opening* [[12]] (For interpretation of the references to colour in this figure legend, the reader is referred to the Web version of this article.)

Undoubtedly, the flow characteristics around the building and near-façade are integral to natural ventilation. Recently published wind tunnel and LES studies on SS2 visualized and demonstrated the interconnection between the pumping flow frequency and the fluctuating characteristics of the flow around the building, e.g., vortex-shedding [15,36,37]. The Strouhal number (*St*), defined as the normalized vortex shedding frequency according to the building height and mean velocity at that height, $St = f_s.H/U_H$, is an essential indicator of the periodic fluctuations in the interaction between the flow field and a bluff body. This value for a finite wall-mounted cube has been reported by previous studies (0.13 [38] and 0.145 [39]). Along with the periodic features of the fully turbulent flow around a finite wall-mounted cube, the presence and nature of parallel near-façade flow (i.e., downwash, upwash and transversal flows) are of major significance in SSV studies. Previous studies have reported parallel near-façade flow for a finite wall-mounted cube and infinite cylinder [35,40–42]. Previous LES studies assessed the moderate Reynolds number flow characteristics between two high-rise buildings and reported the presence of upwash, downwash and transversal near-façade flows [43]. The near-façade parallel flow on both windward and leeward sides of a finite wall-mounted cube with a single door-shaped opening can also be observed in previous Particle Image Velocimetry study results [11].

1.2. Aims of the study

The evidence of the above findings illustrates the importance of a better understanding of near-façade flow in performance evaluations of SSV in order to provide early-stage guidance to building designers on how to exploit this ventilation method better.

The main aims of the work reported here were:

I. To evaluate the external flow and near-façade flow characteristics around a cubic, isolated scaled model of a three-storey building.
II. To investigate how the interconnected relationship between near-façade flow and local flow at the opening affects the ventilation performance of SSV.
III. To assess how the coupling approach can be employed to explain geometrical and aerodynamical phenomena in SSV.

1.3. Proposed contribution

Given the complexity of the flow structures in single-sided ventilation and its low-impact ventilation performance, there is a need to conduct a study focused on the fundamental characteristics of the flow in this type of ventilation. This paper makes several contributions to the literature. Firstly, to the authors' knowledge, this is the first study investigating the *coupled* nature of the external and internal flow in wind-dominant SS1, explicitly evaluating phenomena such as the presence of the mixing layer, short-circuiting and the role of near façade pressure. Secondly, the study provides a detailed evaluation of the ventilation performance effect of the opening position on the building façade, which can fundamentally affect, and shed light on, the interpretation of discrepancies in the performance of SS1 by researchers and designers. Third and finally, the findings of the study provide useful early-stage guidance to building and component designers on how to better exploit this ventilation approach.

1.4. Organisation and structure of the paper

The main scope of this study is on the fundamental flow characteristics in wind-dominant single-sided NV. The methodology section (Section 2) includes computational geometry details and boundary conditions, numerical schemes and algorithms, wind loads and pressure calculations, grid study, and flow rate calculations in the CFD. The results of the present study are provided in section 3. This section includes the validation results, near-façade flow characteristics, and evaluation of the coupling of external and internal flows in SSV. Discussions on indoor secondary flow in SSV and the flow rate at the opening with different positions on the building façade are provided in section 4. The practical implications of the study are discussed in section 5. The final section (section 6) contains conclusions.

2. Methodology

2.1. Computational geometry and boundary conditions

A generic surface-mounted cube was used to represent the scaled model of a three-storey building with SS1 rooms at different positions on the building façade (Fig. 2). The floor areas ($H/2 \times H$) and heights ($H/3$) in all rooms in Fig. 2 (c and d) are the same. The case with an opening on the second floor only on the leeward side in Fig. 2 (b) is used for validation and internal flow distribution evaluations. It is similar in floor area, ($H \times H$), and opening size, ($H/6 \times H/3$)), to the case evaluated in the wind tunnel study of Zhong et al. [37]. Note that all the rooms in Fig. 2 are single-sided, and in Fig. 2 (d), the rooms are completely separated by an interior wall (no interior connection and air transmission). Note that single-sided rooms with openings on both windward and leeward façades were considered in the evaluations. Table 1 summarises the various cases evaluated in the study. Regarding the naming of each case study, "C" refers to the cases with an opening located at the centre of the building façade, i.e. Fig. 2 (c); "S" refers to the cases with two side openings, i.e. Fig. 2 (d); "WW" or "LW" refers to windward or leeward façades, respectively; and "2″ in CLW2 in Table 1 means only the second floor has an opening for the validation case.

Table 1 clarifies the purpose of the study adopted for each case illustrated in Fig. 2. To assist with discussions and analyses in the paper, the case labels in Table 1 will be referred to in all figures and explanations hereafter. After running a grid study on bluff body cases, the case with the optimum grid size is used to validate the mean streamwise velocity profiles on the wake side of the cube with the previous wind

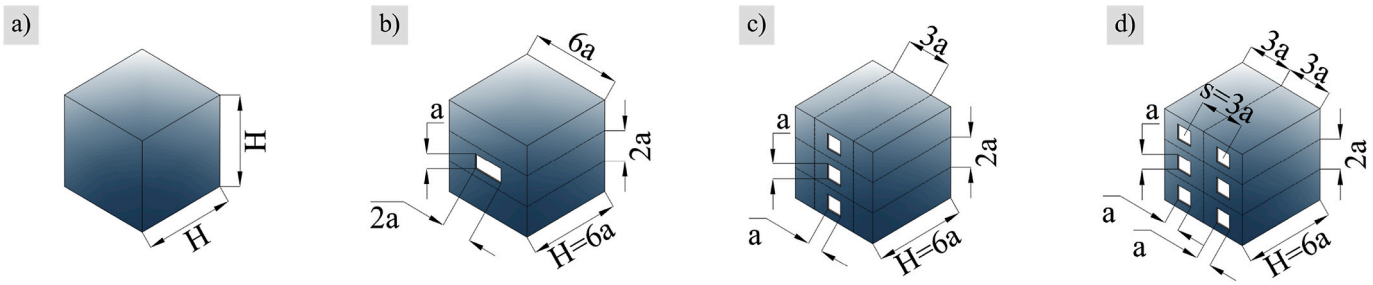

Fig. 2. a and b) the geometries of the reduced scale models based on the wind tunnel study of Zhong et al. [37], c and d) geometries of reduced scale case studies in the present study; H = 300 mm. Note: cases (c) and (d) were assessed for both windward and leeward wind directions.

Table 1
The case studies assessed for different purposes in the present study.

Case No.	Case Label	Case tag in Fig. 2	Purpose of study
1	Bluff Coarse	a	Grid study
2	Bluff Medium	a	Grid study, validation, and flow characteristics study
3	Bluff Fine	a	Grid study
4	CLW2	b	Tracer gas decay method ventilation rate validation
5	CWW	c	Main Study (i.e. coupling internal/external flows in SS1)
6	CLW	c	Main Study (i.e. coupling internal/external flows in SS1)
7	SWW	d	Main Study (i.e. coupling internal/external flows in SS1)
8	SLW	d	Main Study (i.e. coupling internal/external flows in SS1)

tunnel study of Zhong et al. [37]. In addition, further assessments were completed using this case for validation purposes and near-façade flow characteristics studies. Note that the opening and room dimensions in cases CWW, CLW, SWW, and SLW were chosen to keep the same opening area to floor area ratio of 5.56% as the case CLW2, which was the case investigated in the wind tunnel measurements [37]. In cases SWW and SLW, the rooms were entirely separated by a wall between the rooms on the same floor.

The domain size, grids, and boundary conditions (Fig. 3) were determined based on the best practice guidelines [44–46].

The inlet, outlet, and lateral boundaries are at a distance of 5H, 15H, and 5H from the cubic building (see Fig. 3 (a)). The determined distances of the lateral and top boundaries will lead to a 1.5% blockage ratio, below the maximum recommended blockage ratio of $\beta = 3\%$ to avoid too strong artificial acceleration of the flow due to strong contraction of the flow by these boundaries [46].

The boundary conditions in the present study were applied based on the wind-tunnel study of Zhong et al. [37] (see Table 2).

The inlet boundary condition was determined based on the measured velocity and turbulence intensity profiles provided by the wind-tunnel study of Zhong et al. [37]. Although the wind tunnel measurements reported a power-law inlet profile of $U/U_H = (z/H)^{0.19}$ [37], this profile is presented as a logarithmic profile to specify the profile of turbulence dissipation rate based on Richards and Hoxey [47] and the profile of turbulent kinetic energy based on Tominaga et al. [45]. The logarithmic velocity, turbulence kinetic energy, and turbulence dissipation rate profiles were applied at the inlet boundary based on Eqs. (2)–(4),

$$U(z) = \frac{u^*_{ABL}}{\kappa} ln\left(\frac{z+z_0}{z_0}\right) \quad (2)$$

$$k(z) = (U(z)I_u(z))^2 \quad (3)$$

$$\varepsilon(z) = \frac{\left(u^*_{ABL}\right)^3}{\kappa(z+z_0)} \quad (4)$$

where u^*_{ABL}, the atmospheric boundary layer friction velocity, is 0.47 m/s, κ, von Karman constant, is 0.41, and z_0, aerodynamic roughness

Table 2
Adopted boundary conditions in the present study.

Boundary Label in Fig. 3	Boundary Name	Purpose of study
A	Inlet	Logarithmic velocity inlet
B	Lateral and Top	Zero-shear stress
C	Outlet	Zero gradient
D	Ground	No-slip
E	Building	No-slip

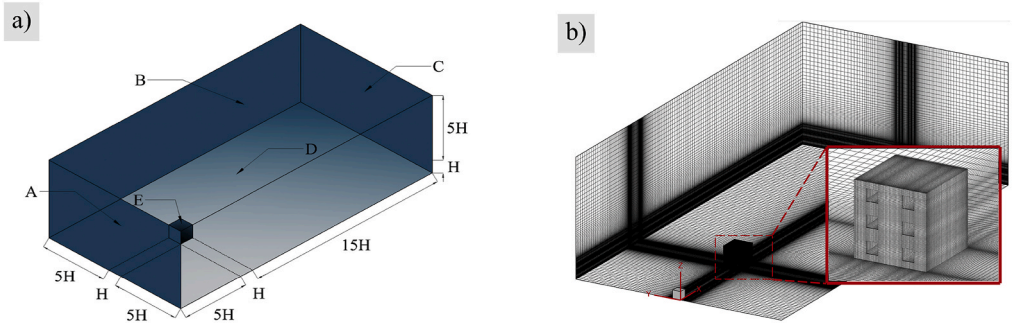

Fig. 3. a) Computational domain with dimensions, H = 300 mm, b) example of the adopted non-uniform structured and orthogonal grid for case SWW.

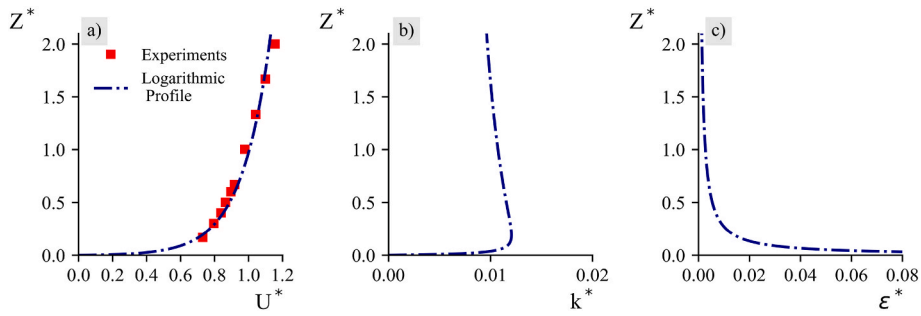

Fig. 4. (a) Normalized mean logarithmic profile in the present study (dash-dot line) and the experimental measurements (red squares) by Zhong et al. [37], (b) Normalized turbulent kinetic energy profile, and (c) normalized turbulent dissipation profile applied in the present study at inlet boundary. (For interpretation of the references to colour in this figure legend, the reader is referred to the Web version of this article.)

length, is 0.0008 m. The R–squared value for the best fit of the logarithmic profile is 0.97. In Eq. (3), the best-fit profile of measured turbulence intensity [37] was determined as $I_u(z) = 0.1(z/H)^{-0.233}$ with $R^2 = 0.95$. Turbulence intensity in the present study refers to the ratio of the root-mean-square of the velocity fluctuations to the mean flow velocity. The resulting profiles are illustrated in Fig. 4. It is noteworthy to mention that the incidence angle of inlet velocity was zero (see Eq. (2)), and the reference velocity at the building height, U_H, was 6.76 m/ s. The adopted profiles at the inlet boundary are illustrated in Fig. 4.

In the present study, a Fourier-based synthetic turbulence generator (STG) [48] is adopted to generate time-dependent inlet conditions for scale-resolving turbulence simulations.

Zero-gradient (pressure and velocity) and zero-shear stress boundary conditions were applied to the outlet boundary and lateral and top boundaries, respectively. No-slip boundary conditions and Werner-Wengle wall functions [49] were adopted for the building and ground. This wall function was also adopted in previous LES studies on bluff body simulations [50], natural ventilation [51], and near-façade flow characteristics assessments [52].

The results and analysis have been evaluated on horizontal surfaces at the centre of each opening at $Z^* = 0.167, 0.500, 0.833$ (see Fig. 5 (a)). These assessments were also carried out on vertical surfaces at $Y^* = 0.00, 0.25$ (see Fig. 5). In order to evaluate the flow structures at the opening and inside the building, the geometries have also been cut through the cross sections at $Y^* = 0.0$ and $X^* = 5.5$ (see Fig. 5).

2.2. Governing equations, numerical schemes and algorithms

All numerical simulations were carried out using the commercial software package ANSYS FLUENT 2021R1 [53]. Pre-processing, i.e., grid generation was done by ICEM CFD 2021R1 [54]. Post-processing, including visualization of the CFD results and generating graphs, was done by Tecplot 2021 [55] and Matplotlib [56].

In LES, the larger three-dimensional unsteady turbulent motions are directly resolved, although the smallest resolvable eddies are limited by

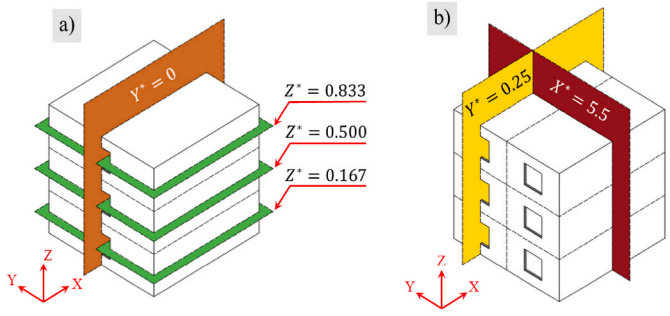

Fig. 5. Planes of analysis and the cross section cuts in the results.

grid spacing and hence the computer power [57–59]. Fortunately, experiments indicate that small scales of turbulence approach isotropy and thus can be modelled [59]. Therefore, in the LES, the exact solution is decomposed into a large-scale and a sub-grid scale components [57]. Because the large-scale unsteady motions are represented explicitly, LES can be expected to be more accurate and reliable than RANS models for flows in which large-scale unsteadiness is significant – such as the flow over bluff bodies, which involves unsteady separation and vortex shedding [58]. The flow characteristics' basic assumptions for solving grid-filtered momentum and continuity equations are three-dimensional incompressible constant properties of Newtonian viscous flow [58,60,61].

The WALE (wall-adapting local eddy viscosity) was adopted as the sub-grid scale modelling. By applying the WALE SGC model, neither the damping function (e.g., Van Driest exponential damping function in Smagorinsky SGC model) nor the dynamic procedure (e.g., dynamic Smagorinsky-Lily model) is needed, although the required grid resolution for proper LES resolving near walls makes using a wall function necessary [33].

As the number of grid nodes increases significantly in near-wall resolved LES for high-Reynolds-number flows, it is considered impractical for high-Reynolds-number flows, e.g., aeronautical and meteorological applications [58]. Therefore, the proper wall function was adopted to reduce the effect of the Reynolds number on the number of cells. Investigation of the effectiveness of different combinations of SGS models and wall-functions in simulating separation from a curved surface found that the combination of Werner-Wengle wall-law and the WALE models gives the closest comparison to the highly resolved simulation [62].

The accurate second-order scheme of the bounded-central difference was applied to approximate the diffusion and advection fluxes, and the second-order scheme was exploited for temporal discretization. The pressure and velocity distribution coupling was obtained using the SIMPLE algorithm [63,64]. The convergence criterion of the residuals was set to reduce to less than the threshold of 10^{-6} for continuity and momentum equations.

The constant time-step size of 4×10^{-4} (s) or a normalized time-step ($\Delta t^* = \Delta t U_H/H$) of 0.009 was adopted. This time-step size also leads to the maximum Currant-Friedrichs-Lewy number less than one, $CFL_{max} = max\left[\Delta t\left(\sum_{i=1}^{n}\frac{u_i}{\Delta x_i}\right); n = 1,2,3\right] < 1$ [65], everywhere in the computational domain, through the simulation process. The same order of magnitude of this time-step has been adopted in previous studies of atmospheric boundary layer wind tunnel simulations using the LES method [11,36,51,66–68]. All cases were run for 20,000 initial time steps (16 vortex-shedding periods); then, the averaging process for all cases was continued for at least 70,000 time-steps (56 vortex-shedding periods). Accordingly, two nodes of the supercomputer, which is a cluster of 336 nodes where each has 2 × 20-core 2.4 GHz Intel Xeon Gold 6148 processors at the Irish Centre for High-End Computing (ICHEC)

[69] were employed to solve the flow field at each time-step for the whole computation process.

2.3. Wind loads and pressure

The present study employed the drag coefficient (C_D) and lift coefficient (C_L) calculation formula based on Yan and Li [70] (Eqs. (5) and (6)) as the approaching wind profile is not uniform,

$$C_D = \frac{F_D}{0.5\rho H \int_0^H U(z)^2 dz} \tag{5}$$

$$C_L = \frac{F_L}{0.5\rho H \int_0^H U(z)^2 dz} \tag{6}$$

where ρ is the air density, $U(z)$ is the mean wind speed corresponding to the height z, and F_D and F_L are forces acting parallel and transverse to the streamwise flow direction, respectively. These equations are similar to the $C_D = F_D/0.5\rho\overline{U}^2H^2$ [71] when the inlet velocity is uniform. Hence, the pressure coefficient in the present study was calculated by the same averaging method as Eq. (7),

$$C_P = \frac{P - P_0}{0.5\frac{\rho}{H}\int_0^H U(z)^2 dz} \tag{7}$$

where $P - P_0$ is the gage pressure.

2.4. Grid study

In LES, the filtered Navier-Stokes equations were solved to resolve those eddies larger than the filter size and model those smaller than the filter size (which can be the grid size) by sub-grid scale modelling. Eighty per cent of the turbulent kinetic energy can be resolved when the ratio of the length scale of turbulence to the filter size is roughly equal to 12 ($\frac{L}{\Delta} \cong 12$) for the sharp cut-off filter and $\frac{L}{\Delta} \cong 17$ for the Gaussian filter in the case of a high Reynolds number [58]. A criterion for examining sufficient LES grid resolution based on the average of this recommended ratio ($\frac{L}{\Delta} \cong \frac{12+17}{2} = 14.5$) was adopted by previous studies [72]. This criterion is recommended everywhere in the domain for near-wall resolved LES and everywhere away from walls for near-wall modelled LES. Given the relationship between integral length scale λ and the length scale of turbulence L , $\lambda = 0.55L$, this criterion means that there should be at least eight cells to resolve an eddy of size λ to be able to achieve the 80% resolving of turbulent kinetic energy. Although the criterion of sufficient grid resolution for LES is straight forward, it can be fulfilled by various grid sizes; some studies have used RANS results of the same geometry to find the proper grid resolution for LES [73]. Three different non-uniform structured and orthogonal grids with different first grid sizes (δ/H) were adopted for this grid study (see Table 3). The maximum growth rate of the grid was set to be 7% for all cases, and the maximum aspect ratio was 20.

The variations in mean drag coefficient, $\overline{C_D}$, and Strouhal number, St, from the coarse mesh to medium mesh are 6% and 7.69%, respectively; and from medium mesh to fine mesh are 3% and 7%, respectively (see Table 3). Note that, due to differences in the boundary layer thickness and Reynolds number of the different studies, reporting a relative error is not an appropriately comparable measure; however, the comparisons in Table 3 can indicate values in the acceptable range. Hence, the medium mesh selected in the present study is the optimum mesh in terms of computational cost and the accuracy of predicting the global values and flow structures around the bluff body.

2.5. Tracer gas decay method simulations

To carry out the tracer-gas decay method to find the effective ventilation rate and the amount of air that short-circuits in SS1, the dispersion of the gas tracer was modelled by the convection-diffusion passive scalar equation for incompressible turbulent flows [61,75,76]. The Turbulent Schmidt number, which is related to the prediction of eddy diffusivity, was set to 1 [75] in the present study.

The volume-averaged value of the calculated CO_2 concentration inside the room in case CLW2 was recorded throughout the simulation at each time step, t_i, by LES; the ventilation rate based on the decay method when the background ventilation is zero was calculated simultaneously using Eq. (8) [20,30],

$$Q_t = \frac{-ln(C_{t_{i+1}}/C_{t_i}).V}{t_{i+1} - t_i} \tag{8}$$

And the value of the effective ventilation rate can be calculated using Eq. (9) [30],

$$Q_{mean} = V.Slope \tag{9}$$

where V is the room volume, and the *Slope* is the slope of the decay graph when there is linear decay.

2.6. Flowrate calculation in CFD simulation

Based on Jiang et al. [77], the airflow rate into or out of a building can be calculated by integrating the normal velocity at all openings if the flow is incompressible, which is true in most natural ventilation studies. Based on a mass balance of the airflow within a building, the total amount of airflow out of a building is equal to the total amount of airflow into a building; therefore, the mean flow rate can be calculated by Eq. (10) [77],

$$Q_{mean} = \frac{1}{2}\sum_{j=ja}^{jb}\sum_{k=ka}^{kb}\left|U_{j,k}\right|\Delta y_j \Delta z_k \tag{10}$$

where $(\Delta y_{ja}, \Delta y_{ja+1}, .., \Delta y_{jb})$ and $(\Delta z_{ja}, \Delta z_{ja+1}, .., \Delta z_{jb})$ are grid sizes in the y and z directions within the opening. $U_{j,k}$ is the mean normal velocity corresponding to the grid $(\Delta y_j, \Delta z_k)$ at the opening. The computed airflow rate in a building is called the mean flow rate, Q_{mean}. This formula calculates the airflow rate by integrating the time-averaged normal velocities over the opening area.

As LES can provide the instantaneous velocity field at each time step, the airflow rate into a building can also be calculated by accumulating and averaging the instantaneous ventilation rate over a time period of T;

Table 3
Mean drag coefficient, mean lift coefficient, and Strouhal number for three bluff bodies of difference grid sizes.

Case label	$Re_H \times 10^{-5}$	Method	δ/H	$n_x \times n_y \times n_z$	$\overline{C_D}$	$\overline{C_L}$	St
Bluff-Coarse	1.2	LES	0.013	181 × 144 × 95	1.041	0.00	0.108
Bluff-Medium	1.2	LES	0.01	218 × 168 × 112	1.108	0.00	0.117
Bluff-Fine	1.2	LES	0.0067	275 × 200 × 132	1.144	0.00	0.126
[39]	0.8 – 1.15*	Exp.	–	–	–	–	0.145
[38]	10^{-3} – 3.4	Exp.	–	–	–	–	0.13
[35]	0.4	LES	–	210 × 66 × 114	1.166	–	0.146
[74]	0.22	Exp.	–	–	0.95	–	–

*This range is based on the channel height.

the accumulative instantaneous ventilation rate over a time period of T, Q_t, is defined as Eq. (11) [77],

$$Q_t = \frac{\frac{1}{2}\sum_{n=1}^{N}\left(\sum_{j=ja}^{jb}\sum_{k=ka}^{kb}\left|u_{j,k}^{n}\right|\Delta y_j \Delta z_k\right).\Delta t^n}{\sum_{n=1}^{N}\Delta t^n} = \frac{\frac{1}{2}\sum_{j=ja}^{jb}\sum_{k=ka}^{kb}\sum_{n=1}^{N}\left|u_{j,k}^{n}\Delta t^n\right|\Delta y_j \Delta z_k}{T} \quad (11)$$

where $u_{j,k}^{n}$ is the instantaneous velocity at the opening at the time t^n, Δt is the time step size ($t^{n+1} - t^n$), N is the total number of time steps during which Q_t was calculated.

The method of cumulating and averaging the air change rate (ACR) values derived from integrating the instantaneous opening velocities will overpredict the room ACR for all wind directions. It is apparent that not all the airflow entering a room can effectively eliminate overheated or polluted indoor air, as some of the incoming air leaves the room immediately after entering. Notwithstanding the reported inaccuracies, the present study adopted this method for a relative comparison the flow numbers in rooms in case studies, as it has been adopted in many CFD studies of SSV [75,77,78]. Note that the short-circuiting phenomenon in case CLW2 was evaluated using the tracer gas method, although adopting the tracer gas method for all cases was out of the scope of this study.

3. Results

Demonstrating the validation results, this section includes near-façade flow features, short-circuiting, and opening position effect evaluations. Given the presence of parallel near-façade flow, further evaluations were completed to investigate the interconnection between external and internal flow in SSV. In order to do this, time-averaged and instantaneous contours and streamlines are illustrated. The effective ventilation rate using the tracer gas decay method and the CO_2 contours inside the building results in investigations on the short-circuiting phenomenon and the secondary flow inside the building. The effect of opening position on ventilation rate and pressure's role on flow rate discrepancies were also evaluated in this section.

3.1. Validation with wind-tunnel experimental data

The mean streamwise velocity profiles on three vertical and three horizontal lines on the wake of the case "Bluff-Medium" have been compared (Fig. 6) with experimental wind-tunnel measurements [37]. The predicted mean streamwise velocity profiles demonstrate similar trends with good agreement with the measured velocity profiles in the wind tunnel. To evaluate this quantitatively, two validation metrics, the factor of 2 of observations (FAC2) and the factor of 1.3 of observations (FAC1.3), were adopted [79]. These metrics were defined based on Eqs. (12) and (13). Metrics such as the normalized mean square error (NMSE) and the fractional bias (FB) cannot be adopted for this evaluation when the velocity reaches both positive and negative values [79,80]. The resulting values are reported in Table 4.

$$FAC2 = \frac{1}{N}\sum_{i=1}^{N} n_i \quad with\ n_i = \begin{cases} 1 & for \quad 0.5 \le \frac{P_i}{O_i} \le 2 \\ 0 & for \quad else \end{cases} \quad (12)$$

$$FAC1.3 = \frac{1}{N}\sum_{i=1}^{N} n_i \quad with\ n_i = \begin{cases} 1 & for \quad 0.77 \le \frac{P_i}{O_i} \le 1.3 \\ 0 & for \quad else \end{cases} \quad (13)$$

Both horizontal and vertical streamwise velocity profiles in Fig. 6 show the negative mean streamwise velocities for the region where lines are on the wake of the building, which shows the presence of the reverse flow. Out of the shear layer, streamwise velocities increase considerably

Table 4
Quantitative evaluation of the validation of LES results of mean streamwise velocity for U/U_H.

	Ideal value	Vertical lines on the wake			Horizontal lines on the wake		
		Line A	Line B	Line C	Line D	Line E	Line F
FAC2	1	0.75	1	1	0.89	0.89	0.89
FAC1.3	1	0.63	0.88	1	0.78	0.89	0.89

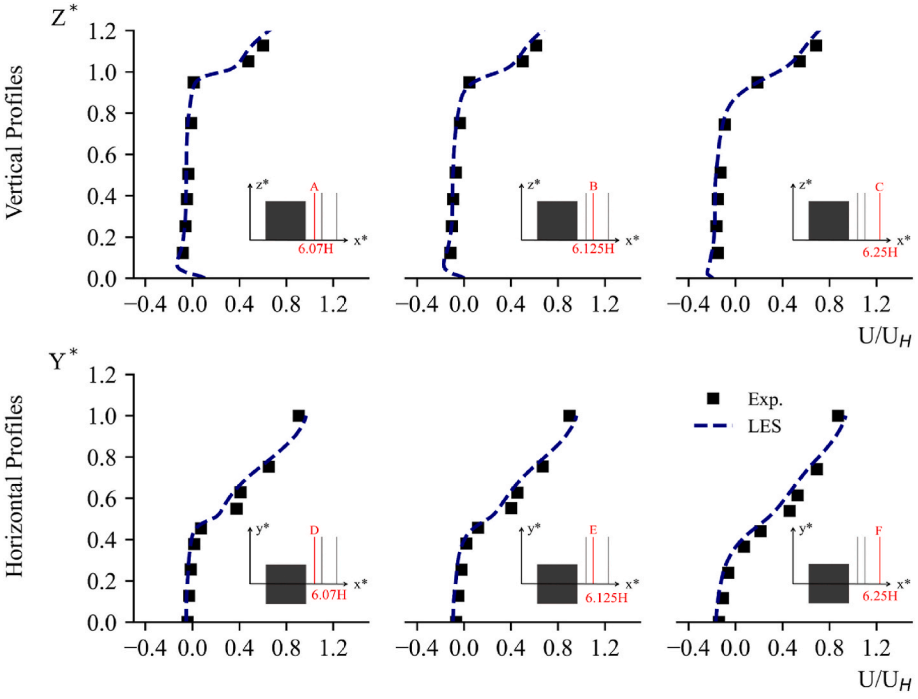

Fig. 6. Validation of the resulted mean streamwise profiles on the wake side of the building on three vertical and horizontal lines in the present study with wind-tunnel measurements [37].

on vertical lines due to shear layer separation from the top leading edge and on the horizontal lines due to separation on the side leading edges.

The mean streamwise velocities are in good agreement with measurements, although other aspects must be assessed to show the robustness of the present LES model. For the "Bluff-Medium", which is the grid applied on all cases with different geometries, the lift coefficient is zero due to symmetrical simulations, the drag coefficient of 1.108 and Strouhal number of 0.136 are in the range of the reported values in the literature for the finite wall-mounted cube (see Table 3). These results indicate that a finite wall-mounted cubes pressure fluctuations and frequency spectrum have been predicted accurately.

As mentioned, the velocity-based method for calculating the ventilation rate (i.e., the calculation method in Eq. (11)) might not agree with the experimental prediction because of the short-circuiting phenomenon. Therefore, one of the cases from the wind tunnel study of Zhong et al. [37] (CLW2, case b in Table 1) was simulated using the tracer gas decay method with LES to show the validity of the predicted effective ventilation rate compared to the reported results by wind-tunnel measurements. The slope of the line in the linear decay region for the tracer gas decay method shows good agreement with the effective ventilation rate measured and reported in the wind tunnel, with a modest 4.49% relative error observed in Fig. 7 (a).

The resulting dimensionless flow number ($F_r = Q/U_H A$), of the tracer gas method, was found to be 0.019 and can be considered as an effective flow number along with the flow number calculated by Eq. (11) as 0.032 (see Fig. 7 (b)). Comparing these values as normalized effective ventilation rate and normalized flow rate at the opening can provide the percentage of the flow rate at the opening that contributes to the effective ventilation rate in the room. The results in Fig. 7 show that 59.4% ($\cong \frac{3}{5}$) of the flow rate at the opening contributes to the effective ventilation rate, and 40.6% ($\cong \frac{2}{5}$) of the flow rate at the opening short-circuits in single-sided natural ventilation. Similar values of the fraction of short-circuiting of the airflow in single-sided natural ventilation have been noted in previous studies [81].

Not only are the results of the mean streamwise velocity profiles and effective ventilation rate values validated with the wind tunnel results, but also the parameters such as drag coefficient and Strouhal number and the fraction of short-circuiting of the air at the opening are in good agreement with the previously reported results. Given that the LES model has been shown to provide reliable results, the near-façade flow characteristics will be assessed in the next section.

3.2. Near-façade flow characteristics

To investigate the cause for the presence of local parallel flow at the opening in SS1, the focus in this section is on recognising the near-façade flow patterns in the case "Bluff-Medium". Then, a detailed assessment of the local flow structure at the opening will be undertaken in the following sections. The time-averaged pressure coefficient contours and time-averaged streamlines on the building faces for the case "Bluff-Medium" are demonstrated in Fig. 8. Local parallel near-façade flow directions can be observed in Fig. 8. The reporting of local parallel flow at the opening in previous field measurements (Fig. 1) can be interpreted by evaluating Fig. 8. The flow arriving at the cube, which is representative of a three-storey building without any openings, on the windward side on average furcates from the stagnation point. In other words, the average position of the stagnation point ($Y^* = 0, Z^* = 0.67$) on the front face is the result of a balance between upwash, downwash, and transversal flows on this face. There exists a downwash flow from the stagnation point to the bottom edge of the building close to the ground, and there exists an upwash flow to the leading top edge of this face (Fig. 8). Moving from the stagnation point to side leading edges of the front face $Y^* = (-0.5, 0.5)$, there exist transversal flows. All these streams extend to the side vertical leading edges and top leading edge of the building. This separation will cause a pressure drop (shown by the blue colour in Fig. 8); further, due to the separation effects on the side edges and corresponding pressure drop, two symmetric separation bubbles are formed and consequently, this causes parallel reverse flows (Fig. 8, Left and Right faces). Given that these shear layers' momentum cannot overcome the main stream's momentum, reattachments of the flow can be seen on the left and right faces. Similar, though not the same separation and reattachment effect, is the form of the flow structures on the top face (see Fig. 8). Two counter-rotating vortices with the same boundary on the symmetry line of the flow are responsible for the reverse flow on the wake. Once this reverse flow reaches the rear face, it forms a local highest-pressure point that acts like the stagnation point on the front face. On the rear face, due to the position of the local highest-pressure ($Y^* = 0, Z^* = 0.083$), the upwash flow is the dominant near-façade flow direction. Obviously, because of the symmetric inflow ($\overline{C}_L = 0$), the stagnation point/local highest-pressure point is located at the symmetry line of the building.

The pressure coefficient and streamlines illustrated in Fig. 8 are time-averaged values; however, the flow around the building and near-façade is turbulent, three-dimensional, and periodic. The time-averaged streamlines and time-averaged pressure coefficient contours result from statistical averaging of these flow characteristics. Given the critical role of instantaneous and periodic flow features, more details will be evaluated in the following sections.

3.3. Coupling external and internal flows in SSV

The general structure of the flow at the opening in SSV has been described as a *mixing layer* by previous studies [22,81,82]. A jet of air tilted towards the room is formed in SSV due to the presence of adjacent parallel flows with different velocities (internal flow and near-façade flow) at the same boundary (opening) [81]. For this reason, the focus of the investigations revolves around the presence of parallel near-façade flow and the effect of this on the flow at the opening and the secondary internal flow.

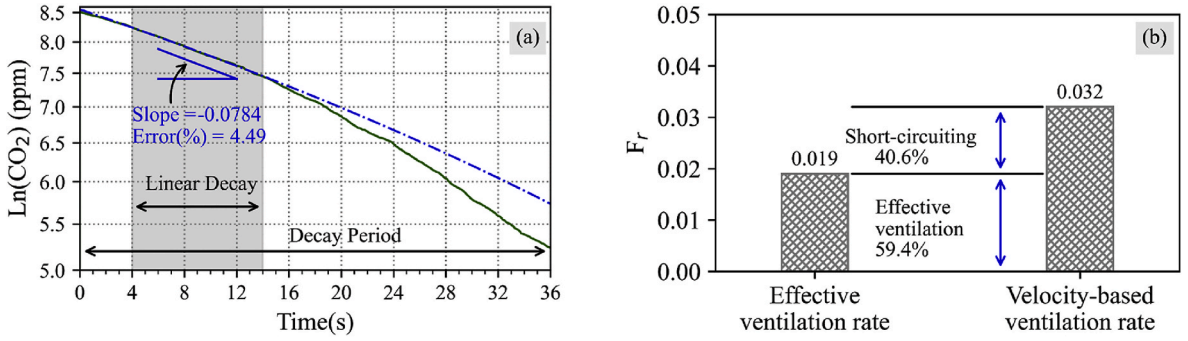

Fig. 7. (a) Tracer gas decay process, (b) comparison of the effective ventilation rate (tracer gas decay method) and ventilation rate (velocity-based method), both calculated by the results of LES.

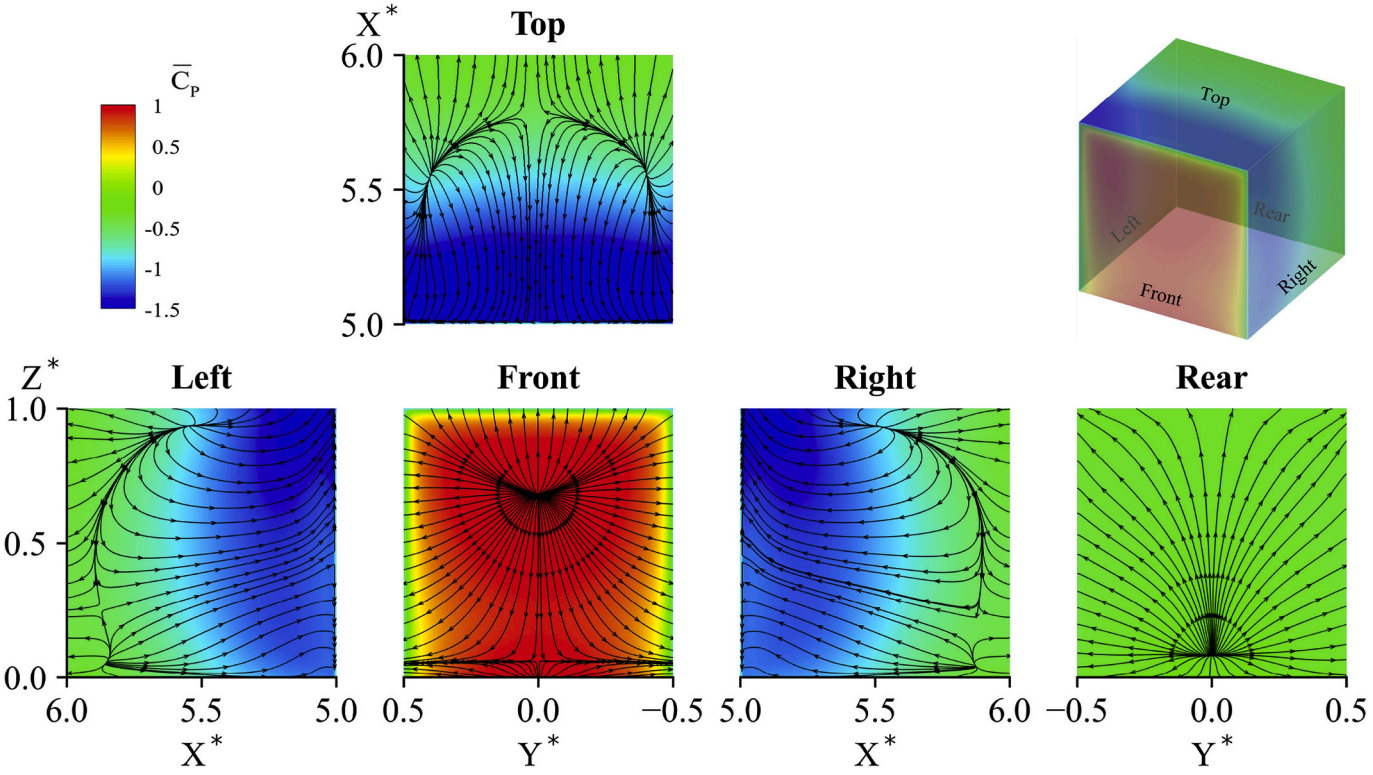

Fig. 8. Time-averaged pressure coefficient contours and time-averaged near-facade streamlines on the case Bluff-Medium.

To identify the details of the flow characteristics present in coupled external and internal flows, in this section, time-averaged and instantaneous streamlines, time-averaged and instantaneous vorticity contours, time-averaged pressure coefficients, and time-averaged Q-Criterion iso-surfaces are evaluated for cases CWW, CLW, SWW, and SLW.

The time-averaged y-vorticity ($\overline{\omega}_y{}^*$) and time-averaged streamlines for case CWW on the symmetry plane ($Y^* = 0$) are shown in Fig. 9 (e). Note that the planes of analysis, $Y^* = 0$ and $Y^* = 0.25$ in all cases in Fig. 9 are demonstrated in the 3D schematic in Fig. 5. Downwash and upwash flows furcating from the stagnation point show similar behaviour as described in Fig. 8. Using y-vorticity to assess the interaction of the near-façade flow and the openings (Fig. 9(a–d)) shows the flow enters the opening in the form of a jet tilted towards the room [81]. As this jet of air interacts with the opening, there is an increase in instantaneous and time-averaged y-vorticity ($\omega_y{}^*, \overline{\omega}_y{}^*$) which shows the increase in velocity gradients in the flow direction. The results for the leeward side in the case CLW (Fig. 9 (f)) show the same feature, as there is upwash flow from the local highest-pressure point ($Y^* = 0, Z^* = 0.062$) to the top edge of the leeward side of the building façade.

As described, the structures of the inlet jet in cases CWW and CLW can be interpreted by the same principles. However, some differences should be considered in assessing these cases regarding the position of the openings. The flow jet entering the room has a higher tilt at openings 2 and 3 in the case CWW compared to the same openings on the leeward side for the case CLW and opening 1 in the case CWW. The first difference between these openings, as the reason for the higher tilt towards the room, can be explained according to the surface averaged mean pressure coefficient and RMS pressure coefficient on the opening plane ($\overline{C}_{PS}$, $C_{PS_{RMS}}$). As shown in the time-averaged streamlines on vertical surfaces illustrated in Fig. 9 (i and j) and based on Table 5, the higher the near-façade pressure value, the higher the jet is tilted towards the room. Evaluating Table 5 for cases CWW and CLW shows that the RMS pressure coefficient is higher when the opening position is closer to the maximum pressure position. For cases with side openings on the building façade on both the windward and leeward sides (SWW and SLW), the same characteristics of the flow as cases CWW and CLW can be seen in Fig. 9 g, h, k, and l. The $\overline{C}_{PS}$ and $C_{PS_{RMS}}$ values are reported in Table 5.

As mentioned in the previous sections, all the flow characteristics in this geometry are three-dimensional. Therefore, further assessment of the observed jet has been carried out on the horizontal planes (parallel to the ground surface, see Fig. 5) at the centre of the opening ($Z^* = 0.167, 0.500, 0.833$) for each case, shown in Fig. 10; which shows time-averaged z-vorticity ($\overline{\omega}_z^*$) contours and time-averaged streamlines. Note that the planes of analysis, $Z^* = 0.167, Z^* = 0.500$, and $Z^* = 0.833$ in all cases in Fig. 10 are demonstrated in the 3D schematic in Fig. 5.

As it is shown by $\overline{\omega}_z^*$ contours in Fig. 10, the external flow structures around the building in all cases are similar. Two separation bubbles on the sides of the building (due to flow separation from vertical leading edges) reduce in transversal size vertically towards the third floor ($Z^* = 0.833$) due to the moving reattachment point from the trailing edges upstream. Two counter-rotating time-averaged vortices (formed due to vortex shedding) on the wake of all cases diminish when they reach the third floor (near the top of the building) due to strong downwash flow from the shear layer separation. Streamlines on $Z^* = 0.167, Z^* = 0.500$, $Z^* = 0.833$ in all cases in Fig. 10, emphasis on the explanations in Fig. 8. The flow reaches the front face, moves transversally to the edges of this face, and because of the separation, two separation bubbles form, which causes reverse flows on the sides of the building façade. Two counter-rotating vortices on the wake cause transversal flow furcating from the local highest pressure point on this side of the building.

For both cases CWW and CLW, compared with cases SWW and SLW, on the horizontal surfaces, the inlet jet is not the cause of significant increment in $\overline{\omega}_z^*$ (see Fig. 10(a–f)). For instance, $|\overline{\omega}_z^*|$, averaged on the opening surface of the second floor, for CWW, CLW, SWW, and SLW are 0.024, 0.12, 1.556 and 0.602, respectively. The openings in cases CWW and CLW are placed precisely on the symmetry line of the flow structures on both sides. Hence the transversal flow has not reached to higher velocity, and the upwash or downwash flows play the dominant role at this position on the building façade. Based on the information obtained

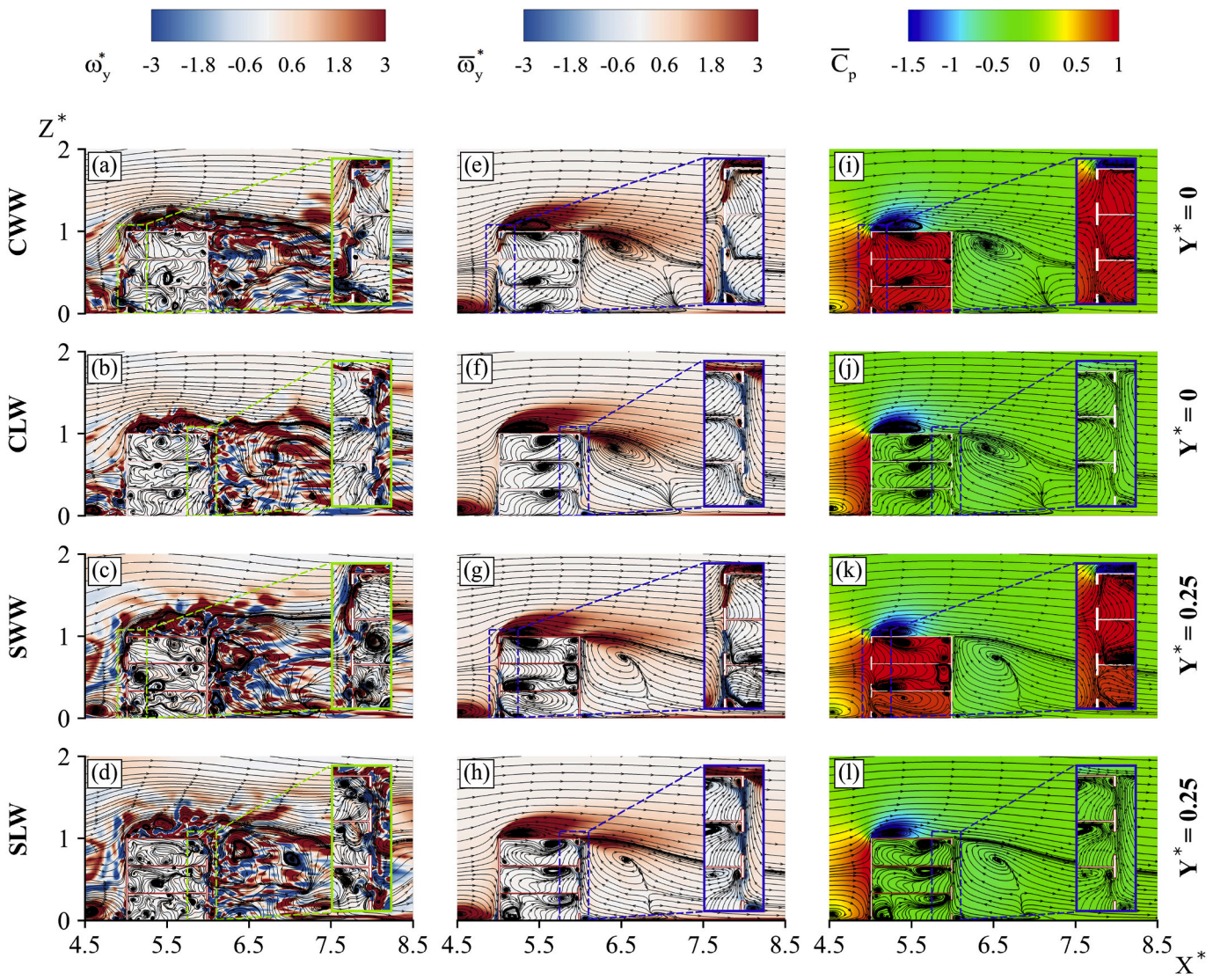

Fig. 9. (a–d) Instantaneous streamlines and instantaneous y-vorticity contours, (e–h) time-averaged streamlines and time-averaged y-vorticity contours, (i–l) time-averaged streamlines and time-averaged pressure coefficient contours, on the vertical surfaces at the centre of the openings. The long-dashed boxes show zoomed contours.

from Figs. 9 and 10 for cases CWW and CLW, assuming a 2D structure for the inlet jet as assumed in the previous studies in SS1 [22,81], can be a correct assumption on this particular opening position. However, the structure of the inlet jet is 3D in essence. On the other hand, investigating the shape of the jet for cases SWW and SLW, which demonstrated the same characteristics on vertical surfaces as the inlet jet with cases CWW and CLW (Fig. 9), the inlet jet on the horizontal surfaces in cases SWW and SLW reveals new features in Fig. 10 (g–l). As the position of the openings in cases SWW and SLW allow the transversal flows to reach their higher velocity gradient, there is an increment in the z-vorticity at these openings. Therefore, when the openings are located far from the symmetry line of the flow structures, assuming "*the jet of fluid tilted towards room*" as a 2D jet is inaccurate. This is because the transversal flow's effect is comparable to the upwash and downwash flow's effect on the flow structure at the opening. Not only does the jet of fluid entering the room tilt toward the room, but it is also inclined based on the position of the opening relative to the stagnation point (more details on the characteristics and shape of this jet will be provided in the following).

Another important point to mention in Fig. 10 (g–l) is the inclination of the jet on horizontal surfaces for cases with side openings. For case SWW, the jet is tilted towards the room with a higher inclination on the third floor than the second floor and a higher inclination on the second floor than the first floor. This emphasises the role of pressure on the inclination of the jet (see Fig. 9 (i–l)). The higher the near-façade pressure, the higher the inclination of the jet. Interestingly, in the case SLW at which the gradient of the near façade pressure is not significant, the jet is inclined towards the room significantly, except for opening 1, which is located close to the local highest pressure point on the leeward façade. All these assessments on the time-averaged pressure and time-averaged vorticity contours and time-averaged streamlines in Figs. 9 and 10 clarify the importance of pressure role in SS1 (more evaluations are provided in the following).

The instantaneous flow features in all four cases, CWW and CLW, on $Y^* = 0$, SWW and SLW on $Y^* = 0.25$, are assessed using the instantaneous y-vorticity (ω_y^*) contours and instantaneous streamlines in Fig. 9 (a–d), and instantaneous z-vorticity contours and instantaneous streamlines along the horizontal planes $Z^* = 0.167$, $Z^* = 0.500$, $Z^* = 0.833$ in Fig. 11. In addition, the periodic behaviour of the instantaneous pressure and the instantaneous vortex structures, which are important in describing the discussed phenomena at the opening, has been illustrated in Fig. 12 schematically. Note that the planes of analysis, $Z^* = 0.167$, $Z^* = 0.500$, and $Z^* = 0.833$ in all cases in Fig. 11 are demonstrated in

Table 5
Surface averaged RMS pressure coefficient and mean pressure coefficient at the openings on floors 1, 2, and 3 in all cases (CWW, CLW, SWW, SLW).

		RMS Pressure Coefficient ($\overline{C}_{PS}$)	Mean Pressure Coefficient ($C_{PS_{RMS}}$)	Max Pressure Position on the Building Façade with Opening		
				X^*	Y^*	Z^*
CWW	Floor 1	0.268	0.921	5.000	0.000	0.685
	Floor 2	0.292	1.043			
	Floor 3	0.328	1.049			
CLW	Floor 1	0.148	−0.293	6.000	0.000	0.062
	Floor 2	0.147	−0.336			
	Floor 3	0.153	−0.358			
SWW	Floor 1	0.270	0.833	5.000	0.000	0.705
	Floor 2	0.303	0.978			
	Floor 3	0.330	1.005			
SLW	Floor 1	0.163	−0.324	6.000	0.000	0.088
	Floor 2	0.157	−0.350			
	Floor 3	0.155	−0.360			

the 3D schematic in Fig. 5.

As described in Fig. 9 (e–l) and Fig. 11, the main structure of the flow at the opening in SS1 is a jet of fluid tilted towards the room, typically referred to in the literature as a *mixing layer*. However, the resulting mean values indicated that this jet could be affected by the position of the opening on the building façade and the mean pressure. Fig. 9 (a–d) and Fig. 11 can help to clarify the effect of fluctuating pressure and the role of vortex structures (the size of which are comparable with the opening sizes) on the attenuation of the inlet jet structure. Opening 2 in case CWW and case SWW (Fig. 9 (a and c), Fig. 11 (b and h)) are examples of attenuation caused by fluctuating pressure effects. This is demonstrated schematically in Fig. 12, where the blue dots refer to the instantaneous locations of the stagnation point (the results of at least four vortex-shedding period statistical records). It can be observed in Fig. 12 how the instantaneous highest-pressure coefficient moves periodically on the windward side of the building façade. The statistically averaged location of these points shows the same value as the resulting location of the stagnation point in the time-averaged results ($Y^* = 0$, $Z^* = 0.67$).

An analysis of the instantaneous highest-pressure location of at least four vortex-shedding periods reveals that the instantaneous highest-pressure location's standard deviation in the Y^* direction ($\sigma_{Y^*} = 0.26$) is higher than the deviation in the Z^* direction ($\sigma_{Z^*} = 0.16$). This suggests the locus of vertical and horizontal periodic movements of the instantaneous highest-pressure affects openings 2 and 3 in cases CWW and SWW the most. It is also reasonable to assume that instantaneous transversal parallel flow, discussed previously, is formed due to these movements. This effect, for example, can be seen in Fig. 9 (c), where the location of the separation of flow into downwash and upwash flow is right at the bottom of opening 2. Although the time-averaged streamlines opening 2, in this case, is aerated by a downwash flow, the location of the instantaneous highest-pressure can attenuate the developed shear mixing layer; therefore, the instantaneous pressure plays a vital role in intermittently destabilising the mixing layer. Horizontal shifting of the instantaneous highest-pressure has the same attenuation effect on the structure of the jet at opening 2 in case SWW. In addition to the attenuation effect on opening 2 in case SWW, horizontal movements of the highest-pressure mean that the highest-pressure is located on each of the side openings on floor two and causes a pressure difference between the openings on this floor. This can be the main reason for the phenomenon observed as pumping flow in SS2 in previous studies [36,37]. Although the openings are not connected internally in this study (as in SS2), and a wall entirely separates the rooms, results show that the indoor pressure of the rooms at the same level fluctuates periodically (see Animation 1). This shows the pumping flow in SS2 occurs because of such periodic movements of the instantaneous highest-pressure location.

Opening 1 in cases CWW and SWW (Fig. 9 (a and c)) is an example of the potential attenuation of the inlet jet due to vortex structures with dimensions comparable to the opening size. Instantaneous horseshoe vortex core locus, and front junction vortex core locus, which exhibit reciprocating and rotating movements instantaneously in front of the building, are outlined in Fig. 12. Note that junction vortex refers to a vortex forms at the building wall and ground surface junction. These vortex structures result in the generation of vortices which affect the jet of air entering the room. Nonetheless, due to the strong downwash flow at the location of opening 1 in cases CWW and SWW, the belly shape of deflection in the mean streamlines of the inlet jet cannot be seen in these cases as it can be seen in Fig. 9 (e and g) for opening 2. Opening 1 in case CLW is an example of belly-shaped deflection and attenuation of the inlet jet due to the effect of the highest local time-averaged pressure, periodic movements of the instantaneous highest local pressure of the leeward façade (Figs. 9 and 11), and the presence of the junction vortex (see Fig. 12).

To visualize these vortices and the form of inlet jet, in addition to time-averaged and instantaneous vorticity, pressure and streamlines (Figs. 9–11), the iso-surface of the $\overline{Q}$-criterion for four case-studies (CWW, CLW, SWW, SLW) are assessed in Fig. 13. Note the cross sections in Fig. 13 (a and b) are at $Y^* = 0$, and the cross sections in Fig. 13 (c and d) are at $X^* = 5.5$ (see the 3D schematic in Fig. 5). $\overline{Q}$-criterion is representative of the local balance between shear strain rate and vorticity magnitude. It defines the areas of vortices where the vorticity magnitude is greater than the magnitude of the rate of strain:

$$\overline{Q} = \frac{1}{2}\left(|\overline{\Omega}_{ij}|^2 - |\overline{S}_{ij}|^2\right) > 0 \tag{14}$$

The $\overline{Q}$-criterion iso-surfaces in Fig. 13 are three-dimensional illustrations of the vortex structures such as horseshoe vortex, symmetric vortex bubbles on the wake, and separation bubbles on top and sides of the building. In addition to these vortex structures (also illustrated in Figs. 8–12), vortex structures locally at the opening, which form as the result of coupling external and internal flows, can be seen in Fig. 13. $\overline{Q}$-criterion iso-surfaces in Fig. 13 (a and b) clearly illustrate the shape of the inlet jet in cases with centre openings which are formed as the result of upwash flow (opening 3 in case CWW, and all openings in case CLW) and downwash flow (openings 1 and 2 in case CWW).

Higher deflection at opening 3 of case CWW due to high pressure and higher jet attenuation in opening 2 of case CWW (Fig. 9 (a, e, i), and Fig. 13 (a)), and opening 1 of case CLW (Fig. 9 (b, f, j), and Fig. 13 (b)) can be seen. Indiscrete vortex structures can be observed in opening 1 of case CWW (Fig. 13 (a)) and opening 3 of case CLW (Fig. 13 (b)), which is the result of stronger downwash near-façade flow, and stronger upwash near-façade flow, respectively. This shows that the higher the parallel near-façade flow velocity, the stronger the mixing layer of the jet at the opening, despite all attenuating parameters. The three-dimensional illustration of the inlet jet at the opening for the cases with the centre opening (Fig. 13 (a and b)) appears to verify the assumption that the jet across the opening in SS1 is a 2D structure and this can be acceptable as discussed above by evaluating the instantaneous and time-averaged y-vorticity and z-vorticity components.

The main point to note about the cases with side openings (SWW and SLW) in Fig. 13 (c and d) is the direction of the inlet jet. In case SWW, the inlet jet angle towards the opening is a function of both spanwise (upwash/downwash) and transversal flows (see Fig. 13 (c), Fig. 9 (c, g, k), Fig. 10 (g, h, j)). According to the previously mentioned physical evidence, the structure of the inlet jet locally at the opening is three-dimensional for cases with side openings. Therefore, it can no longer be assumed that a 2D mixing layer is interacting with the opening.

In addition, there are external flow structures that can be seen in Fig. 13. The horseshoe vortex exists upstream of the building and is extended to the downstream side of the building on the wake. This horseshoe vortex is illustrated in Fig. 9 (i, j, k, l). Another flow structure

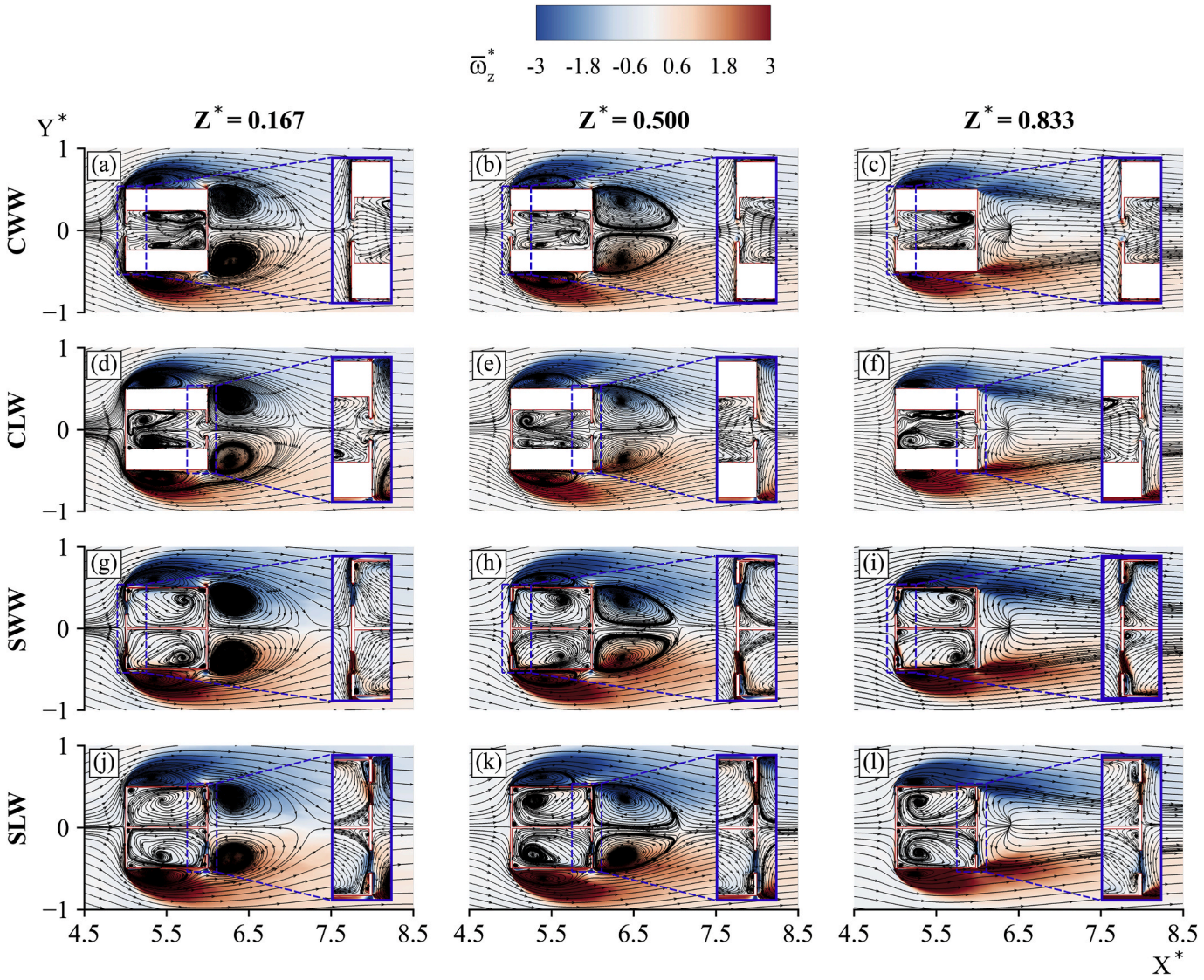

Fig. 10. Time-averaged z-vorticity contours and time-averaged streamlines on the horizontal surfaces at the centre of the openings in cases CWW, CLW, SWW, and SLW. The long-dashed boxes show zoomed contours.

that can be observed is the recirculation region on the top face which forms due to separation at the leading edge of this face. This separation and reattachment on the top face are also demonstrated in Fig. 12. Front and rear junction vortices on the front and rear sides of the building close to the bottom edges of the front and rear faces form close to the ground (Fig. 12 demonstrates the instantaneous locus of these junction vortices). The effect of these two junction vortices is also shown on the front and rear faces of the building in Fig. 8. Finally, the separation and reattachment phenomena occurred on the side faces of the building in all case studies.

4. Discussion

Detailed assessments of the flow structures in the near-building façade region and locally at the opening in SS1 clarify that the flow structure in SS1 is a three-dimensional jet of fluid. This jet is formed as the result of parallel near-façade flow locally at the opening with the angle of attack related to the position of the opening and the location of the maximum pressure on that façade. This jet can be deflected towards the room due to the local near-façade pressure. This jet can also be attenuated or deflected due to periodic pressure fluctuations and/or vortex structures with sizes comparable to the opening size at a particular location. As well as understanding the interactions of near-façade flow and the flow locally at the opening in SSV, it is also essential to evaluate the system's performance in terms of indoor air distribution and the effect of opening position.

4.1. Indoor secondary flow in SS1

One of the critical aspects of the performance of a ventilation system is indoor air distribution. The aim of ventilation is to provide comfort and wellbeing for the occupants, although controlling the indoor air distribution in a system such as SSV, in which a single opening plays both extract and supply air roles, appears very challenging. Nevertheless, understanding the coupling between indoor air distribution and the near-façade flow can provide a more holistic insight in terms of any performance evaluation in a system such as SS1.

The circulations inside the rooms are a function of the direction of the inlet jet at the opening (see Figs. 9–11). For example, in room 2 of case CLW, the upwash near-façade flow causes the jet of air to enter the room from the bottom edge of the opening to the top edge, moving towards the ceiling. In wind-dominant natural ventilation, the inlet jet is the source of fresh outdoor air and is the main driving force of secondary air circulation inside the room. It can be expected that the air inside the

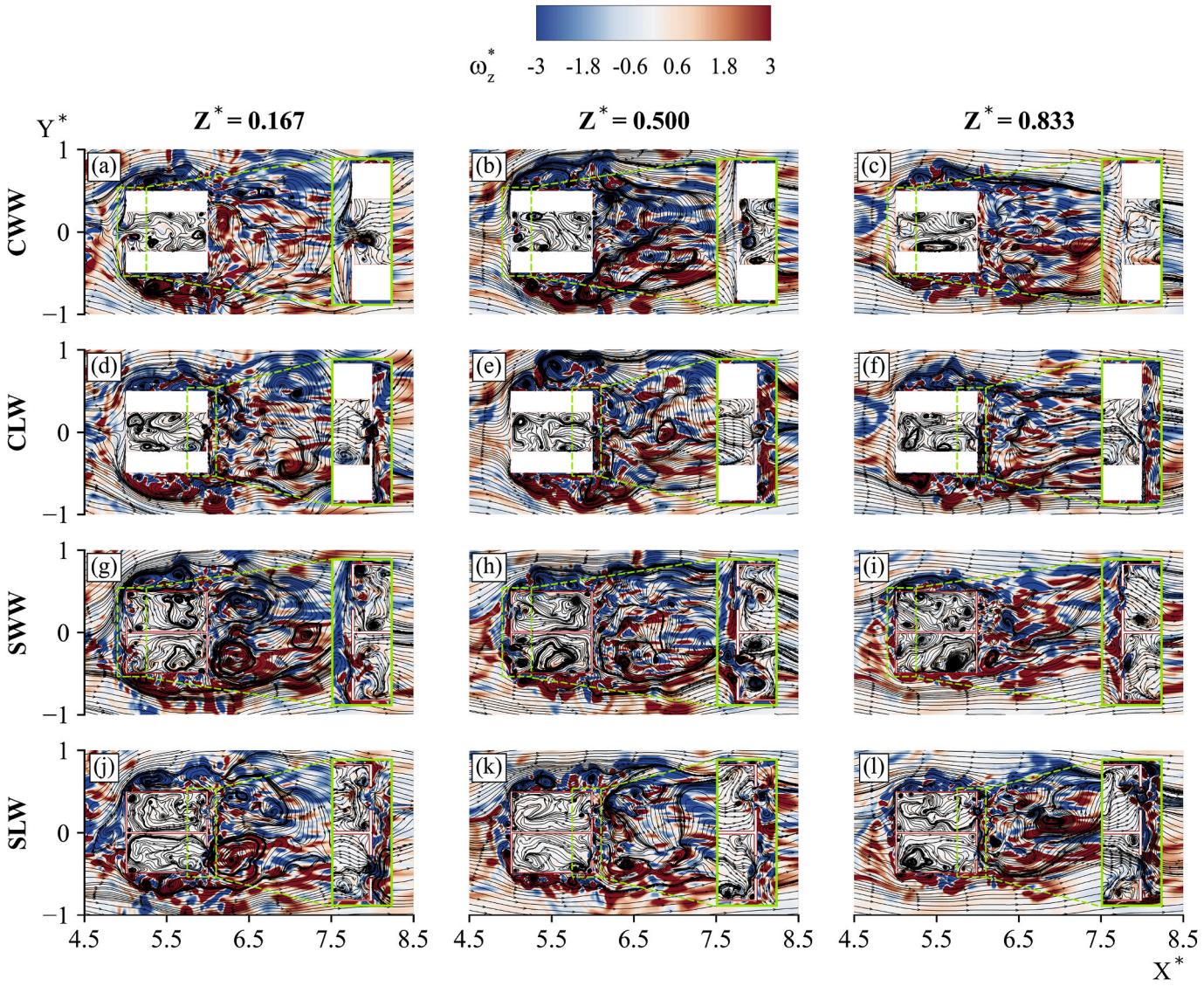

Fig. 11. Instantaneous z-vorticity contours and instantaneous streamlines on the horizontal surfaces in cases CWW and CLW and in cases SWW and SLW. The long-dashed boxes show zoomed contours.

room will be non-isotopically distributed, i.e., more fresh air near the ceiling and more aged air near the ground. The contours of instantaneous CO_2 concentration inside the room in case CLW2 (see Fig. 14) that showed the short-circuiting phenomenon in the previous section confirm this interpretation. The instantaneous CO_2 concentration contours in the case CLW2 through time are demonstrated in Fig. 14. T^* represents the nondimensional time, normalized by the air change rate (ACR (1/s)) calculated based on the tracer gas decay method (see Fig. 7). For example, $T^* = 0.94$ determines the contours that are representative of CO_2 concentration after almost one air change.

As illustrated in Fig. 14, the inlet jet of fresh air enters the room from the bottom edge of the opening, moving towards the top edge and the ceiling close to the opening. This direction of the inlet jet in the wind-dominant SS1 system, in this case with the opening at the centre of the leeward façade, causes a higher concentration of CO_2 near the floor where occupants are located. The existing coupling between indoor air distribution and near-façade flow and the dependency of the jet at the opening on the position of the opening relative to the building façade signifies the fact that conclusions on the performance of the wind-dominant SS1 systems can be made more accurately by stating the position of the opening on building façade and the direction of the mainstream in both field measurements and CFD studies.

4.2. *Flowrate at the openings with different positions on the building façade*

The results of flow numbers, F_r, calculated based on the velocity component normal to the opening (Eq. (11)), are highlighted in Fig. 15 for all cases (CWW, CLW, SWW, and SLW). As it is shown in Fig. 15 (a), for the case CWW, the velocity-based flow number increases from the first floor to the third floor. The increment rate is 10%, meaning that the flow number on the second floor is 10% higher than that of the first floor, and it is 10% higher on the third floor than the value of the flow number on the second floor. While for the case CLW, the flow number exhibits a decreasing trend from the first floor to the third floor, and the decreasing rate is not linear.

As discussed in the previous sections, pressure plays a significant role in the deflection of the jet of the air at the opening. As the near-façade flow in cases with a centre opening is dominated either by upwash or downwash flows, the dominant local velocity component at the opening is the z-velocity component. However, the x-velocity component, which is normal to the opening plane, is the main component by which, in Eq.

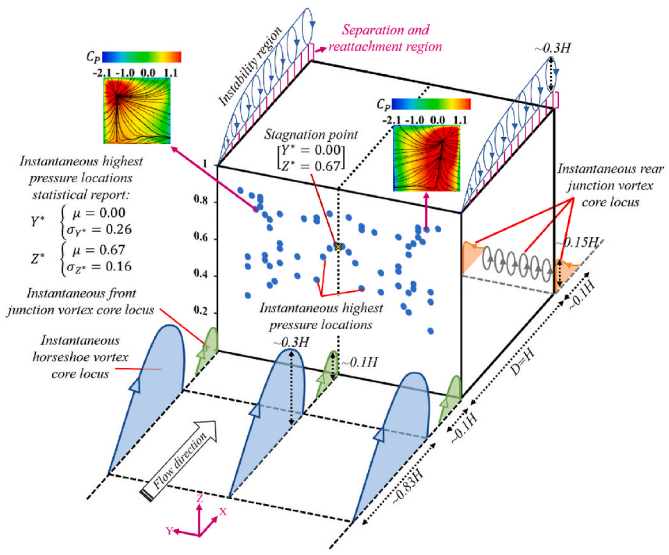

Fig. 12. Schematic illustration of the instantaneous stagnation points on the windward side of the "Bluff-Medium" and evaluated external flow structures.

(11), the flow rate and, consequently, the flow number were calculated. Jet deflection, or how much the mixing layer jet is tilted towards the room, is the main feature of the flow at the opening that transforms the z-velocity (or y-velocity) components into x-velocity components. As described, pressure plays a vital role in deflecting the mixing layer jet. Hence, the increasing rate of the F_r from the first floor to the third floor can be explained by time-averaged pressure increment on the windward side as one of the reasons for this phenomenon. The increasing rate of time-averaged pressure coefficients at the centre line of the openings in case CWW matches the increasing trend of the flow number demonstrated in Fig. 16 (a). The decreasing rate of pressure coefficient can be seen in Fig. 16 (b), which matches the decreasing rate of the flow number in Fig. 15 (b). The time-averaged pressure difference can be adopted as the reason for the decreasing rate of F_r from the first floor to the third floor in case CLW.

As mentioned above, due to the short-circuiting phenomenon in SS1, the ventilation rates calculated by Eq. (11) overpredicts the effective ventilation rate because only about 60% of the flow at the opening contributes to the effective ventilation (Fig. 7 (b)). The effective ventilation rates for all openings in the centre of the leeward façade reported by Zhong et al. [37] show the same decreasing trend from the first to the third floor.

Comparing velocity-based flow rates in case CLW2, which has an opening size of 0.05 m × 0.1 m (see Fig. 2), and $F_r = 0.032$ (see Fig. 7), with the opening on the second floor in case CLW, which has an opening size of 0.05 m × 0.05 m (see Fig. 2), and $F_r = 0.024$ (see Fig. 15), shows the increment in width of the opening causes an increment in F_r. Previous studies have shown that the longer width of the opening changed the characteristics of the air exchange rate [82]. Again, this can be interpreted by the interconnected relationships between the near-façade flow and its effect on the flow locally at the opening and the secondary internal flow. The longer width of the opening at the centre of the façade benefits from both upwash flows and transversal flows. This means the jet of air entering the room no longer has a 2D characteristic, and there will be a three-dimensional flow approaching both the vertical edges of the opening as well as the top edges of the opening. This can also change the airflow distribution inside the room. Detailed assessments of the effects of opening geometry with spanwise and transversal 3D near façade flow require further investigations using the coupling approach.

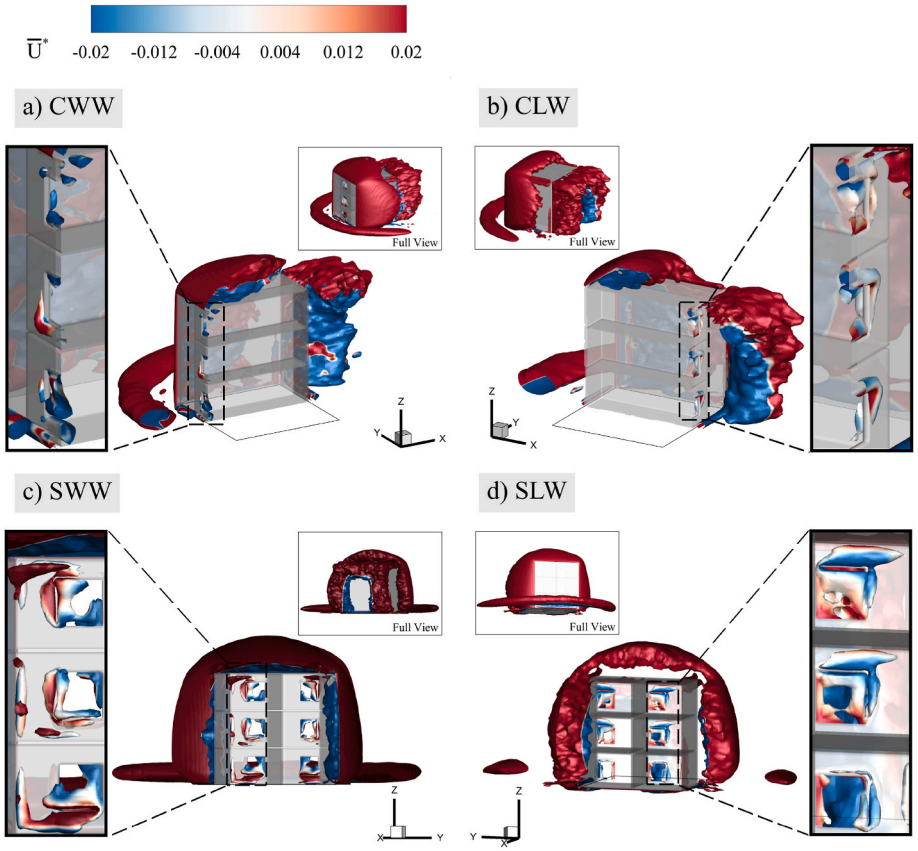

Fig. 13. $\overline{Q}$- criterion of value 0.005 for all case studies coloured by normalized streamwise velocity (CWW, CLW, SWW and SLW) - The cross sections in (a) and (b) is at $Y^* = 0$, and the cross section in (c) and (d) is at $X^* = 5.5$.

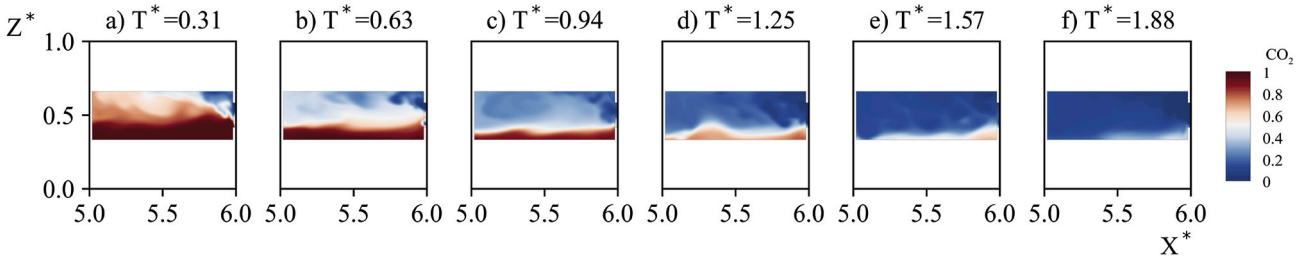

Fig. 14. Instantaneous CO_2 concentration contours for the case with only the second floor and the opening on the leeward side, CLW2, through the time.

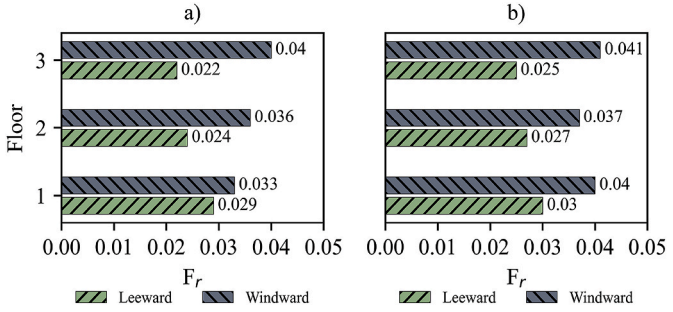

Fig. 15. Flow number (F_r) calculated based on the velocity component normal to the opening plane for a) cases CWW and CLW, b) cases SWW and SLW.

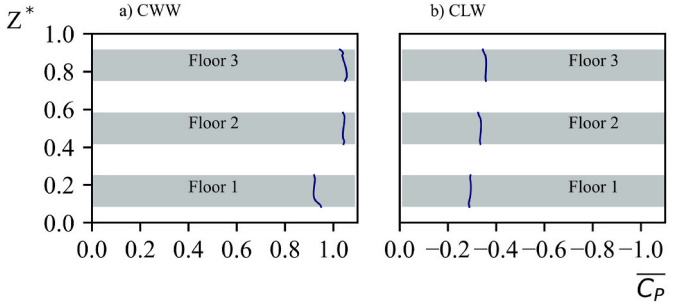

Fig. 16. Mean pressure coefficient graphs at the centre of each opening a) in the case with the centre opening on the windward façade (CWW), b) in the case with the centre opening on the leeward façade (CLW).

5. Practical implications

In a practical sense, a better understanding of the effects of coupling between external and internal flows can assist architects, natural ventilation engineers and researchers improve their designs or research interpretations.

5.1. Performance improvement solutions in architectural design for natural ventilation

The shapes and forms we observe in nature, such as rivers and mountains, are created over long periods by the forces present in the wind and water. Thus, it is possible to design shapes and forms that amplify and work in harmony with the impacts of such natural forces [83]. For example, studies that investigated the effect of building geometry and airflow guiding components, e.g., louvres, and guide vanes, in cross ventilation showed that aerodynamic and geometric evaluations would result in better design and, therefore, better performance of a ventilation system [84–86]. The evaluating approach to coupled external and internal flows in single-sided natural ventilation is a powerful technique for understanding the interaction of the building with airflow-guiding components to design more effective natural ventilation systems.

In some building designs having a room with the opening(s) on only one side of the building façade is inevitable. Whether the building's ventilation is fully or partially dependent on natural ventilation, improving this worst-performing natural ventilation system, i.e., SSV, is crucial. The interaction of the guide vane as an airflow-guiding component with the pure parallel near-facade flow is visualized by a previous wind tunnel study (see Fig. 17) [82].

The presence of a guide vane as an air flow guiding component can cause the deflection of the inlet jet into the room, which in some cases can increase the ventilation rate significantly (up to 11 times higher compared to the plain opening [82]) (see Fig. 17). The characteristics of the near-façade flow shown previously identified the directional nature of parallel flow at ventilation openings beyond transversal alone. To enhance the flow rate inside the room, it is essential to have guide vanes with the proper orientation with respect to the near-façade flow to reach the maximum possible flowrate enhancement. Not only does the magnitude and direction of the incident wind change, but the dominant near-façade flow direction also changes with respect to the opening position on the building façade. This leads to a question; how can a component be designed at the opening to mitigate the variations in the parameters and provide better indoor air quality for all building rooms compared to a building with a plain opening? Further assessments are required to answer this question. Based on the results of the present study, understanding near-façade flow and the interconnected relationship between external and internal flows can be a crucial approach to designing such components.

5.2. Experimental measurements in single-sided natural ventilation

Considering field measurements and wind-tunnel studies as the two main experimental methods in assessing natural ventilation, some details should be included in future experimental studies when reporting results.

The near-façade flow is parallel to the building façade but at different directions to the opening, i.e., as the result of upwash, downwash, and transversal flows. Therefore, reporting the opening(s) position on the building façade, the dominant wind direction (at the reference height), and the local wind direction at the opening, in field measurements will provide useful information for interpreting the results. For example, if an SS1 study with an opening located at the centre of the leeward facade shows that the concentration of the CO_2 close to the floor level is higher than that close to the ceiling, adding the details about the opening position is essential. Such information will clarify the air distribution could be different if the measurements were carried out simultaneously in another room with the same geometry but a different opening position on the building façade.

Wind direction and opening position are always available in wind tunnel measurements. The CFD studies using various geometries to study more details of indoor flow characteristics, pollutant dispersion, and other aspects of the performance of a natural ventilation system should acknowledge that based on the opening position and the interaction of the scaled model of the building with the mainstream flow the

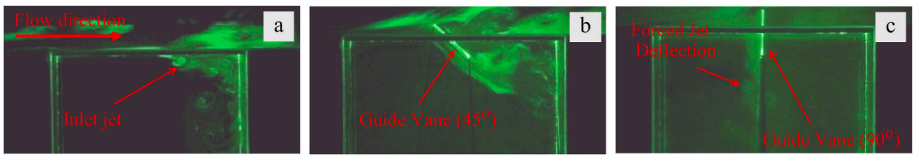

Fig. 17. Flow visualization of the interaction of a guide vane acting as an airflow guiding component with the pure parallel flow in previous wind tunnel studies [82] (red colour annotations by the present study). (For interpretation of the references to colour in this figure legend, the reader is referred to the Web version of this article.)

interpretation of the results could be different. For example, if the scaled model is a cube with a single door (e.g., the wind tunnel study by Jiang et al. [11]), acknowledging the position of the opening is essential in CFD analysis in this case. The opening in the study by Jiang et al. [11] is affected by downwash flow on the windward side. On the leeward side, upwash flow, the location of the highest-pressure point and the rear junction vortex will affect this opening.

6. Conclusions

This paper presented a detailed wind-dominant single-sided natural ventilation analysis using a validated LES numerical model. An isolated cube, representative of a three-storey building, was used to investigate several scenarios on the windward and leeward sides of the building façade with openings at either the centre or sides of the building façade. The focus of the investigations revolved around the presence of parallel flow near the building façade and the effect this has on the flow structure at the opening as well as the internal secondary flow.

Near-wall modelled large-eddy simulations demonstrated accurate prediction of the measured streamwise velocity profile on the wake of the building, validated with wind tunnel measurements from Zhong et al. [37]. The tracer gas decay results were compared to the measurements in the same wind tunnel study, predicting the effective ventilation rate with only a 4.49% error.

Comparing the simulated effective ventilation rate calculated using a tracer gas decay approach with the ventilation rate calculated based on the velocity vectors normal to the opening plane highlighted an over-prediction in the velocity-based approach. This is because only 3/5 of the flow at the opening contributes to the effective ventilation rate, and 2/5 of the flow at the opening short circuits.

The general characteristics of the local airflow at the opening and inside the room were found to be strongly coupled with the near-façade flow in SSV. This connection was observed via structures such as the mixing layer at the opening, which can be deflected or attenuated by the near-façade pressure and vortex structures close to the opening with comparable scales to the opening size.

The pressure fluctuations on the windward and leeward sides of the building façade clearly showed that the directional nature of the near-façade flow is highly dependent on the periodic characteristics of the interaction of the building as a surface-mounted cube with the atmospheric boundary layer flow. Animation 1 demonstrated how these fluctuations relate to the differentiations in pressure of rooms adjacent to each other at the same floor level and in rooms at different floor levels.

The results demonstrate that considering a *mixing layer* as a 2D vertical jet is acceptable only for the openings on the leeward and windward sides located at the centre line of the building façade. For the openings located away from the centreline, this jet is inclined based on the position of the opening relative to the highest-pressure point, and it must be considered a 3D jet.

CO_2 contours from the tracer gas decay simulations confirmed the interconnected relationship between the near-façade flow and the internal secondary flow within the indoor space. This interconnection results in variations in the indoor distribution of the CO_2 depending on the position of the opening on the building façade. The distribution of the CO_2 throughout the decay period showed how the upwash near-façade flow could dictate the secondary flow inside the room in single-sided natural ventilation. Therefore, it is crucial to consider the position of the opening in interpretations of single-sided natural ventilation studies.

Comparisons between the flow rates in a three-story building with the openings at the centre of the building façade showed that the flow rate at the opening from the first floor to the third floor has an increasing trend on the windward side. In contrast, the flow rate at the opening on the centre of the building façade on the leeward side has decreasing trend from the first floor to the third floor. This shows the importance of the mean pressure role locally at the opening in SSV. Hence, there is a difference in the airflow rate in single-sided ventilation with the different opening positions on the building façade.

A better understanding of the interconnected relationship between the near-façade flow and the internal secondary flow can help engineers and architects to develop airflow-enhancing solutions for SSV. For example, components such as certain window designs or louvres can be seen as aerodynamic airflow guiding components rather than simply as barriers to solar gain, burglary and so on. Further studies are needed to design components such as louvres as aerodynamical components instead of evaluating only the pressure coefficient. This approach could lead to better-performing SSV systems by reducing the short-circuiting phenomenon and providing better indoor air distribution.

Additionally, this study recommends that, for experimental studies, as a parameter, the façade position of the opening under investigation and the direction of the wind must be used in the interpretation of the study observations to clarify the role near-façade flow may have on their findings. For CFD studies that adopt scaled models, communicating details related to the position of the opening on the building facade can help readers better to interpret the results and impact of the respective study.

To further explore the capacity of the approach presented here, adopting experimental measurements with controlled boundary conditions, either in a wind tunnel or in a laboratory setting with near-façade wind generators, is necessary to develop airflow-enhancing solutions in SSV.

In addition to evaluating the airflow-enhancing solutions, due to the limitations in the present study, such as considering only the wind-driven single-sided ventilation and simulating an isolated building, further studies are required to investigate the coupling external and internal flows approach for a building in an urban environment, e.g., street canyon, while considering both wind and buoyancy as the driving forces.

CRediT authorship contribution statement

Nima Najafi Ziarani: Writing – review & editing, Writing – original draft, Visualization, Validation, Software, Methodology, Formal analysis, Data curation, Conceptualization. **Malcolm J. Cook:** Writing – review & editing, Project administration, Methodology, Funding acquisition, Conceptualization. **Farnood Freidooni:** Writing – review & editing, Visualization, Validation, Software, Methodology, Formal analysis, Conceptualization. **Paul D. O'Sullivan:** Writing – review & editing, Visualization, Validation, Resources, Project administration,

Methodology, Investigation, Funding acquisition, Conceptualization.

Declaration of competing interest

The authors declare the following financial interests/personal relationships which may be considered as potential competing interests: Paul D O'Sullivan reports financial support was provided by Science Foundation Ireland.

Data availability

No data was used for the research described in the article.

Acknowledgements

This research was part-funded by Science Foundation Ireland (SFI) through MaREI, the SFI Research Centre for Energy, Climate, and Marine, and especially the Centre for Doctoral Training in Energy Resilience and the Built Environment (ERBE) (grant no: 12/R.C./2302_P2, with supporting funding obtained from UK Engineering and Physical Sciences Research Council (EPSRC) (grant EP/S021671/1).

The authors wish to acknowledge the Irish Centre for High-End Computing (ICHEC) for the provision of computational facilities and support.

Appendix A. Supplementary data

Supplementary data to this article can be found online at https://doi.org/10.1016/j.buildenv.2023.110210.

References

[1] A. Aflaki, N. Mahyuddin, Z. Al-Cheikh Mahmoud, M.R. Baharum, A review on natural ventilation applications through building façade components and ventilation openings in tropical climates, Energy Build. 101 (2015) 153–162, https://doi.org/10.1016/j.enbuild.2015.04.033.

[2] H.Y. Zhong, Y. Sun, J. Shang, F.P. Qian, F.Y. Zhao, H. Kikumoto, C. Jimenez-Bescos, X. Liu, Single-sided natural ventilation in buildings: a critical literature review, Build. Environ. 212 (2022), https://doi.org/10.1016/j.buildenv.2022.108797.

[3] T. Kobayashi, M. Sandberg, T. Fujita, E. Lim, N. Umemiya, Numerical analysis of wind-induced natural ventilation for an isolated cubic room with two openings under small mean wind pressure difference, Build. Environ. 226 (2022), https://doi.org/10.1016/j.buildenv.2022.109694.

[4] E. Tavakoli, A.O. Donovan, M. Kolokotroni, P.D. O'Sullivan, Evaluating the indoor thermal resilience of ventilative cooling in non-residential low energy buildings: a review, Build Environ. (2022), 109376, https://doi.org/10.1016/j.buildenv.2022.109376.

[5] A. O' Donovan, P.D. O' Sullivan, The impact of retrofitted ventilation approaches on long-range airborne infection risk for lecture room environments: design stage methodology and application, J. Build. Eng. 68 (2023), 106044, https://doi.org/10.1016/j.jobe.2023.106044.

[6] D. Park, F. Battaglia, Effect of heat loads and ambient conditions on thermal comfort for single-sided ventilation, Build. Simulat. 8 (2015) 167–178, https://doi.org/10.1007/s12273-014-0200-9.

[7] A.M. Papadopoulos, A. Avgelis, Indoor environmental quality in naturally ventilated office buildings and its impact on their energy performance, Int. J. Vent. 2 (2003) 203–212, https://doi.org/10.1080/14733315.2003.11683665.

[8] P. Stabat, M. Caciolo, D. Marchio, Progress on single-sided ventilation techniques for buildings, Adv. Build. Energy Res. 6 (2012) 212–241, https://doi.org/10.1080/17512549.2012.740903.

[9] T.S. Larsen, P. Heiselberg, Single-sided natural ventilation driven by wind pressure and temperature difference, Energy Build. 40 (2008) 1031–1040, https://doi.org/10.1016/j.enbuild.2006.07.012.

[10] C. Allocca, Q. Chen, L.R. Glicksman, Design analysis of single-sided natural ventilation, Energy Build. 35 (2003) 785–795, https://doi.org/10.1016/S0378-7788(02)00239-6.

[11] Y. Jiang, D. Alexander, H. Jenkins, R. Arthur, Q. Chen, Natural ventilation in buildings: measurement in a wind tunnel and numerical simulation with large-eddy simulation, J. Wind Eng. Ind. Aerod. 91 (2003) 331–353, https://doi.org/10.1016/S0167-6105(02)00380-X.

[12] M. Caciolo, P. Stabat, D. Marchio, Full scale experimental study of single-sided ventilation: analysis of stack and wind effects, Energy Build. 43 (2011) 1765–1773, https://doi.org/10.1016/j.enbuild.2011.03.019.

[13] Z.T. Ai, C.M. Mak, Analysis of fluctuating characteristics of wind-induced airflow through a single opening using LES modeling and the tracer gas technique, Build. Environ. 80 (2014) 249–258, https://doi.org/10.1016/j.buildenv.2014.06.002.

[14] WHO, Natural Ventilation for Infection Control in Health-Care Settings, World Health Organization, 2009. https://apps.who.int/iris/handle/10665/44167.

[15] G. Carrilho da Graça, D.P. Albuquerque, M. Sandberg, P.F. Linden, Pumping ventilation of corner and single sided rooms with two openings, Build. Environ. 205 (2021), 108171, https://doi.org/10.1016/j.buildenv.2021.108171.

[16] H. Wang, Q. Chen, Modeling of the impact of different window types on single-sided natural ventilation, in: Energy Procedia, Elsevier Ltd, 2015, pp. 1549–1555, https://doi.org/10.1016/j.egypro.2015.11.201.

[17] Y. Wei, Z. Guo-qiang, W. Xiao, L. Jing, X. San-xian, Potential model for single-sided naturally ventilated buildings in China, Sol. Energy 84 (2010) 1595–1600, https://doi.org/10.1016/j.solener.2010.06.011.

[18] F. Haghighat, J. Rao, P. Fazio, The influence of turbulent wind on air change rates-a modelling approach, Build. Environ. 26 (1991) 95–109, https://doi.org/10.1016/0360-1323(91)90017-6.

[19] D. Etheridge, Natural ventilation of buildings theory measurement and design, Int. J. Vent. 10 (2012) 405–406, https://doi.org/10.1080/14733315.2012.11683965.

[20] Z.T. Ai, C.M. Mak, Modeling of coupled urban wind flow and indoor air flow on a high-density near-wall mesh: sensitivity analyses and case study for single-sided ventilation, Environ. Model. Software 60 (2014) 57–68, https://doi.org/10.1016/j.envsoft.2014.06.010.

[21] H.K. Malinowski, Wind effect on the air movement inside buildings, in: 3rd International Conference "Wind Effects on Buildings and Structures, 1971. Tokyo, https://www.aivc.org/resource/wind-effect-air-movement-inside-buildings.

[22] P.R. Warren, Ventilation through openings on one wall only, in: Proceedingsof Energy Conservation in Heating, Cooling and Ventilating, 1977. https://www.aivc.org/sites/default/files/members_area/medias/pdf/Airbase/airbase_00026.pdf.

[23] H. Wang, Q. Chen, A new empirical model for predicting single-sided, wind-driven natural ventilation in buildings, Energy Build. 54 (2012) 386–394, https://doi.org/10.1016/j.enbuild.2012.07.028.

[24] T. Yamanaka, H. Kotani, K. Iwamoto, M. Kato, Natural, wind-forced ventilation caused by turbulence in a room with a single opening, Int. J. Vent. 5 (2006) 179–187, https://doi.org/10.1080/14733315.2006.11683735.

[25] J. Zhou, C. Ye, Y. Hu, H. Hemida, G. Zhang, W. Yang, Development of a model for single-sided, wind-driven natural ventilation in buildings, Build. Serv. Eng. Technol. 38 (2017) 381–399, https://doi.org/10.1177/0143624417699658.

[26] E. Simiu, Y. DongHun, Wind Effects on Structures: Modern Structural for Wind, fourth ed., Wiley-Blackwell, 2019 https://doi.org/10.1002/9781119375890.

[27] M. Caciolo, S. Cui, P. Stabat, D. Marchio, Development of a new correlation for single-sided natural ventilation adapted to leeward conditions, Energy Build. 60 (2013) 372–382, https://doi.org/10.1016/j.enbuild.2013.01.024.

[28] H.L. Gough, J.F. Barlow, Z. Luo, M.F. King, C.H. Halios, C.S.B. Grimmond, Evaluating single-sided natural ventilation models against full-scale idealised measurements: impact of wind direction and turbulence, Build. Environ. 170 (2020), https://doi.org/10.1016/j.buildenv.2019.106556.

[29] P.D. O'Sullivan, M. Kolokotroni, A field study of wind dominant single sided ventilation through a narrow slotted architectural louvre system, Energy Build. 138 (2017) 733–747, https://doi.org/10.1016/j.enbuild.2016.11.025.

[30] D. Etheridge, M. Sandberg, Building Ventilation: Theory and Measurement, Wiley, West Sussex, 1996.

[31] Z. Bu, S. Kato, Investigation of ventilation effectiveness for wind-driven single-sided ventilated buildings located in an urban environment, Int. J. Vent. 10 (2011) 19–30, https://doi.org/10.1080/14733315.2011.11683932.

[32] Y. Hu, J. Zhou, G. Zhang, An approach of calculation and analysis of pulsating flow rate of single-sided ventilation due to unsteady wind pressure, Sci. Technol. Built Environ. 25 (2019) 588–599, https://doi.org/10.1080/23744731.2018.1556050.

[33] A. Sohankar, Flow over a bluff body from moderate to high Reynolds numbers using large eddy simulation, Comput. Fluids 35 (2006) 1154–1168, https://doi.org/10.1016/j.compfluid.2005.05.007.

[34] D.A. Lysenko, M. Donskov, I.S. Ertesvåg, Large-eddy simulations of the flow over a semi-circular cylinder at Re = 50000, Comput. Fluids 228 (2021), https://doi.org/10.1016/j.compfluid.2021.105054.

[35] S. Krajnovic, L. Davidson, Large-eddy simulation of the flow around a bluff body, AIAA J. 40 (2002), https://doi.org/10.2514/2.1729.

[36] D.P. Albuquerque, M. Sandberg, P.F. Linden, G. Carrilho da Graça, Experimental and numerical investigation of pumping ventilation on the leeward side of a cubic building, Build. Environ. 179 (2020), 106897, https://doi.org/10.1016/j.buildenv.2020.106897.

[37] H.Y. Zhong, C. Lin, Y. Sun, H. Kikumoto, R. Ooka, H.L. Zhang, H. Hu, F.Y. Zhao, C. Jimenez-Bescos, Boundary layer wind tunnel modelling experiments on pumping ventilation through a three-story reduce-scaled building with two openings, Build. Environ. 202 (2021), 108043, https://doi.org/10.1016/j.buildenv.2021.108043.

[38] T. Nakagawa, Vortex shedding behind a square cylinder in transonic flows, J. Fluid Mech. 178 (1987) 303–323, https://doi.org/10.1017/S002211208700123X.

[39] R. Martinuzzi, C. Tropea, The flow around surface-mounted, prismatic obstacles placed in a fully developed channel flow (data bank contribution), J. Fluid Eng. 115 (1993) 85–92, https://doi.org/10.1115/1.2910118.

[40] B.L. da Silva, R. Chakravarty, D. Sumner, D.J. Bergstrom, Aerodynamic forces and three-dimensional flow structures in the mean wake of a surface-mounted finite-height square prism, Int. J. Heat Fluid Flow 83 (2020), 108569, https://doi.org/10.1016/j.ijheatfluidflow.2020.108569.

[41] T. Uffinger, I. Ali, S. Becker, Experimental and numerical investigations of the flow around three different wall-mounted cylinder geometries of finite length, J. Wind Eng. Ind. Aerod. 119 (2013) 13–27, https://doi.org/10.1016/j.jweia.2013.05.006.
[42] H.C. Lim, T.G. Thomas, I.P. Castro, Flow around a cube placed in a simulated turbulent boundary layer, in: The Fourth International Symposium on Computational Wind Engineering, 2006, in: http://iawe.org/Proceedings/CWE2006/TC1-02.pdf.
[43] F. Freidooni, A. Sohankar, M.R. Rastan, E. Shirani, Flow field around two tandem non-identical-height square buildings via LES, Build. Environ. 201 (2021), 107985, https://doi.org/10.1016/j.buildenv.2021.107985.
[44] J. Franke, A. Hellsten, H. Schlünzen, B. Carissimo, Best Practice Guideline for the CFD Simulation of Flows in the Urban Environment, 2007.
[45] Y. Tominaga, A. Mochida, R. Yoshie, H. Kataoka, T. Nozu, M. Yoshikawa, T. Shirasawa, AIJ guidelines for practical applications of CFD to pedestrian wind environment around buildings, J. Wind Eng. Ind. Aerod. 96 (2008) 1749–1761, https://doi.org/10.1016/j.jweia.2008.02.058.
[46] B. Blocken, Computational Fluid Dynamics for urban physics: importance, scales, possibilities, limitations and ten tips and tricks towards accurate and reliable simulations, Build. Environ. 91 (2015) 219–245, https://doi.org/10.1016/j.buildenv.2015.02.015.
[47] P.J. Richards, R.P. Hoxey, Appropriate boundary conditions for computational wind engineering models using the k-ε turbulence model, J. Wind Eng. Ind. Aerod. (1993) 46–47, https://doi.org/10.1016/0167-6105(93)90124-7, 145–153.
[48] M.L. Shur, P.R. Spalart, M.K. Strelets, A.K. Travin, Synthetic turbulence generators for RANS-LES interfaces in zonal simulations of aerodynamic and aeroacoustic problems, Flow, Turbul Combust 93 (2014) 63–92, https://doi.org/10.1007/s10494-014-9534-8.
[49] H. Wengle, H. Werner, Large-eddy Simulation of Turbulent Flow over Sharp-Edged Obstacles in a Plate Channel, 1993, pp. 192–199, https://doi.org/10.1007/978-3-663-13986-7_26.
[50] W. Rodi, On the simulation of turbulent flow past bluff bodies, J. Wind Eng. Ind. Aerod. (1993) 46–47, https://doi.org/10.1016/0167-6105(93)90128-B, 183.
[51] F. Bazdidi-Tehrani, S. Masoumi-Verki, P. Gholamalipour, Impact of opening shape on airflow and pollutant dispersion in a wind-driven cross-ventilated model building: large eddy simulation, Sustain. Cities Soc. 61 (2020), 102196, https://doi.org/10.1016/j.scs.2020.102196.
[52] X. Zheng, H. Montazeri, B. Blocken, CFD analysis of the impact of geometrical characteristics of building balconies on near-façade wind flow and surface pressure, Build. Environ. 200 (2021), 107904, https://doi.org/10.1016/j.buildenv.2021.107904.
[53] Ansys, Inc. Fluent, 2021.
[54] Inc. Ansys, ICEM CFD, 2021.
[55] Tecplot Ltd., Tecplot 360 (2021). https://www.tecplot.com/.
[56] J.D. Hunter, Matplotlib: a 2D graphics environment, Comput. Sci. Eng. 9 (2007) 90–95, https://doi.org/10.1109/MCSE.2007.55.
[57] P. Sagaut, Large Eddy Simulation for Incompressible Flows – an Introduction, Springer, Berlin, Heidelberg, 2002, https://doi.org/10.1007/978-3-662-04695-1.
[58] S.B. Pope, Turbulent Flows, twelfth ed., Cambridge University Press, 2000 https://doi.org/10.1017/CBO9780511840531.
[59] D.R. Chapman, Computational aerodynamics development and outlook, AIAA J. 17 (1979) 1293–1313, https://doi.org/10.2514/3.61311.
[60] F. Nicoud, F. Ducros, Subgrid-scale stress modelling based on the square of the velocity gradient tensor, Flow, Turb. Combust. 62 (1999) 183–200, https://doi.org/10.1023/A:1009995426001.
[61] ANSYS, ANSYS Fluent User's Guide, Release 2021, vol. 1, 2021.
[62] L. Temmerman, M.A. Leschziner, C.P. Mellen, J. Fröhlich, Investigation of wall-function approximations and subgrid-scale models in large eddy simulation of separated flow in a channel with streamwise periodic constrictions, Int. J. Heat Fluid Flow 24 (2003) 157–180, https://doi.org/10.1016/S0142-727X(02)00222-9.
[63] S. Patankar, Numerical Heat Transfer and Fluid Flow: Computational Methods in Mechanics and Thermal Science, first ed., CRC Press, 1980.
[64] A. Mashhadi, A. Sohankar, Md.M. Alam, Flow over rectangular cylinder: effects of cylinder aspect ratio and Reynolds number, Int. J. Mech. Sci. 195 (2021), 106264, https://doi.org/10.1016/j.ijmecsci.2020.106264.
[65] R. Courant, K. Friedrichs, H. Lewy, On the partial difference equations of mathematical physics, IBM J. Res. Dev. 11 (1967) 215–234, https://doi.org/10.1147/rd.112.0215.
[66] J. Wang, L. Wang, W. Zhang, A projection an-isotropic spectrum method for inflow turbulence of Large Eddy Simulation in natural ventilation of buildings, Build. Environ. 199 (2021), 107834, https://doi.org/10.1016/j.buildenv.2021.107834.
[67] X. Zhang, A.U. Weerasuriya, K.T. Tse, CFD simulation of natural ventilation of a generic building in various incident wind directions: comparison of turbulence modelling, evaluation methods, and ventilation mechanisms, Energy Build. 229 (2020), 110516, https://doi.org/10.1016/j.enbuild.2020.110516.
[68] T. van Hooff, B. Blocken, Y. Tominaga, On the accuracy of CFD simulations of cross-ventilation flows for a generic isolated building: comparison of RANS, LES and experiments, Build. Environ. 114 (2017) 148–165, https://doi.org/10.1016/j.buildenv.2016.12.019.
[69] ICHEC, Irish centre for high-end computing, n.d. https://www.ichec.ie/.
[70] B.W. Yan, Q.S. Li, Inflow turbulence generation methods with large eddy simulation for wind effects on tall buildings, Comput. Fluids 116 (2015) 158–175, https://doi.org/10.1016/j.compfluid.2015.04.020.
[71] B.W. McCormick, Aerodynamics, Aeronautics, and Flight Mechanics, second ed., Wiley, 1994.
[72] I.B. Celik, Z.N. Cehreli, I. Yavuz, Index of resolution quality for large eddy simulations, J. Fluids Eng. Trans. ASME 127 (2005) 949–958, https://doi.org/10.1115/1.1990201.
[73] F. Durrani, M.J. Cook, J.J. McGuirk, Evaluation of LES and RANS CFD modelling of multiple steady states in natural ventilation, Build. Environ. 92 (2015) 167–181, https://doi.org/10.1016/j.buildenv.2015.04.027.
[74] R.J. Martinuzzi, B. Havel, Vortex shedding from two surface-mounted cubes in tandem, Int. J. Heat Fluid Flow 25 (2004) 364–372, https://doi.org/10.1016/j.ijheatfluidflow.2004.02.003.
[75] M. Caciolo, P. Stabat, D. Marchio, Numerical simulation of single-sided ventilation using RANS and LES and comparison with full-scale experiments, Build. Environ. 50 (2012) 202–213, https://doi.org/10.1016/j.buildenv.2011.10.017.
[76] H. Kikumoto, R. Ooka, Large-eddy simulation of pollutant dispersion in a cavity at fine grid resolutions, Build. Environ. 127 (2018) 127–137, https://doi.org/10.1016/j.buildenv.2017.11.005.
[77] Y. Jiang, Q. Chen, Study of natural ventilation in buildings by large eddy simulation, J. Wind Eng. Ind. Aerod. 89 (2001) 1155–1178, https://doi.org/10.1016/S0167-6105(01)00106-4.
[78] Y. Jiang, Q. Chen, Buoyancy-driven single-sided natural ventilation in buildings with large openings, Int. J. Heat Mass Tran. 46 (2003) 973–988, https://doi.org/10.1016/S0017-9310(02)00373-3.
[79] J.F.M. Schatzmann, H. Olesen, COST 732 Model Evaluation Case Studies: Approach and Results, 2010.
[80] K. Kosutova, T. van Hooff, C. Vanderwel, B. Blocken, J. Hensen, Cross-ventilation in a generic isolated building equipped with louvers: wind-tunnel experiments and CFD simulations, Build. Environ. 154 (2019) 263–280, https://doi.org/10.1016/j.buildenv.2019.03.019.
[81] G. Carrilho da Graça, A technical note on simplified modelling of turbulent mixing in wind-driven single sided ventilation, Build. Environ. 131 (2018) 12–15, https://doi.org/10.1016/j.buildenv.2018.01.014.
[82] S. Kato, R. Kono, T. Hasama, R. Ooka, T. Takahashi, A wind tunnel experimental analysis of the ventilation characteristics of a room with single-sided opening in uniform flow, Int. J. Vent. 5 (2006) 171–178, https://doi.org/10.1080/14733315.2006.11683734.
[83] U. Passe, F. Battaglia, Designing Spaces for Natural Ventilation, Taylor and Francis, 2015, https://doi.org/10.4324/9780203583470.
[84] J.I. Perén, T. van Hooff, B.C.C. Leite, B. Blocken, CFD analysis of cross-ventilation of a generic isolated building with asymmetric opening positions: impact of roof angle and opening location, Build. Environ. 85 (2015) 263–276, https://doi.org/10.1016/j.buildenv.2014.12.007.
[85] M. Kouhirostami, Natural Ventilation through Windows in a Classroom (CFD Analysis Cross-Ventilation of Asymmetric Openings: Impact of Wind Direction and Louvers Design) Natural Ventilation through Windows in a Classroom (CFD Analysis Cross-Ventilation of Asymmetric Openings: Impact of Wind Direction and Louvers Design) View Project Advance Modular Housing Design View Project, 2018, https://doi.org/10.6084/m9.figshare.12733031.
[86] J.I. Peren, T. van Hooff, R. Ramponi, B. Blocken, B.C.C. Leite, Impact of roof geometry of an isolated leeward sawtooth roof building on cross-ventilation: straight, concave, hybrid or convex? J. Wind Eng. Ind. Aerod. 145 (2015) 102–114, https://doi.org/10.1016/j.jweia.2015.05.014.